

# Density Functional Theory of Freezing and Phase Field Crystal Modeling

K. R. Elder<sup>1</sup>, Nikolas Provatas<sup>2</sup>, Joel Berry<sup>1,3</sup>, Peter Stefanovic<sup>2</sup>, and Martin Grant<sup>3</sup>

<sup>1</sup>*Department of Physics, Oakland University, Rochester, MI, 48309-4487*

<sup>2</sup>*Department of Materials Science and Engineering and Brockhouse Institute for Materials Research, McMaster University, Hamilton, ON, Canada L8S-4L7 and*

<sup>3</sup>*Physics Department, Rutherford Building, 3600 rue University, McGill University, Montréal, Québec, Canada H3A 2T8*

(Dated: July 16, 2018)

In this paper the relationship between the density functional theory of freezing and phase field modeling is examined. More specifically a connection is made between the correlation functions that enter density functional theory and the free energy functionals used in *phase field crystal* modeling and standard models of binary alloys (i.e., regular solution model). To demonstrate the properties of the phase field crystal formalism a simple model of binary alloy crystallization is derived and shown to simultaneously model solidification, phase segregation, grain growth, elastic and plastic deformations in anisotropic systems with multiple crystal orientations on diffusive time scales.

PACS numbers: 05.70.Ln, 64.60.My, 64.60.Cn, 81.30.Hd

## Contents

<b>I. Introduction</b>	1
<b>II. Density Functional Theory of Freezing</b>	3
A. Single Component System	3
B. Multi-Component System	3
<b>III. Analysis of Free Energy Functionals</b>	4
A. Pure Materials	4
B. Binary Alloys	6
1. Liquid phase properties	6
2. Crystalline phase properties	7
C. Simple Binary Alloy Model	7
1. Solid-solid coexistence	8
2. Solid-liquid coexistence	8
3. Linear elastic constants	9
4. Calculation of phase diagrams	9
<b>IV. Dynamics</b>	9
<b>V. Applications</b>	11
A. Eutectic and Dendritic Solidification	11
B. Epitaxial Growth	12
1. Numerical simulations	13
C. The Role of Dislocations in Spinodal Decomposition	14
1. Numerical Simulations	15
<b>VI. Discussion and Conclusions</b>	15
<b>VII. Acknowledgments</b>	16
<b>A. Numerical discretization Schemes</b>	16
<b>B. Free Energy Functional for a Pure Material</b>	16
<b>C. Simple Binary Alloy Model</b>	18

## References

19

## I. INTRODUCTION

The formalism for calculating equilibrium states was established many years ago by Gibbs, Boltzmann and others. While this formalism has proved remarkably successful there are many systems which never reach equilibrium, mainly due to the existence of metastable or long lived transient states. This is most apparent in solid materials. For example it is very unlikely that the reader is sitting a room containing any single crystals except items produced with considerable effort such as the silicon chips in computers. In fact the vast majority of naturally occurring or engineered materials are not in equilibrium and contain complex spatial structures on nanometer, micron or millimeter length scales. More importantly many material properties (electrical, optical, mechanical, etc.) are strongly influenced by the non-equilibrium structures that form during material processing. For example the yield strength of a polycrystal varies as the inverse square of the average grain size.

The study of non-equilibrium microstructure formation has seen considerable advances through the use of the *phase field* approach. This methodology models the dynamics of various continuum fields that collectively characterize microstructure in phase transformations. For example, phase field or continuum models have been used to simulate spinodal decomposition [1], order-disorder transition kinetics [2], ordering of block-copolymer melts [3], solidification of pure and binary systems [4, 5, 6, 7, 8] and many other systems. In these phenomena the evolution of the appropriate field(s) (e.g., solute concentration in spinodal decomposition) is assumed to be dissipative and driven by minimizing a phenomenological free energy functional [1].

Advances in the phase field modeling of solidification phenomena have followed a progression of inno-

vations, beginning with the development of free energies that capture the thermodynamics of pure materials [4, 5, 6] and alloys [7, 8]. Several modifications were then proposed [9, 10, 11] to simplify numerical simulations and improve computational efficiency. Perhaps the most important innovation was the development of matched asymptotic analysis techniques that directly connect phase field model parameters with the classical Stefan (or sharp-interface) models for pure materials or alloys [12, 13, 14, 15]. These techniques were complemented by new adaptive mesh refinement algorithms [16, 17], whose improved efficiency significantly increased the length scales accessible by numerical simulations, thus enabling the first experimentally relevant simulations of complex dendritic structures and their interactions in organic and metallic alloys [18, 19, 20, 21, 22].

A weakness of the traditional phase field methodology is that it is usually formulated in terms of fields that are spatially uniform in equilibrium. This eliminates many physical features that arise due to the periodic nature of crystalline phases, including elastic and plastic deformation, anisotropy and multiple orientations. To circumvent this problem traditional phase field models have been augmented by the addition of one or more auxiliary fields used to describe the density of dislocations [23, 24, 25] continuum stress and strain fields [26, 27] and orientation fields [28, 29, 30]. These approaches have proven quite useful in various applications such as polycrystalline solidification [24, 28, 29, 30, 31, 32]. Nevertheless it has proven quite challenging to incorporate elasto-plasticity, diffusive phase transformation kinetics and anisotropic surface energy effects into a single, thermodynamically consistent model.

Very recently a new extension to phase field modeling has emerged known as the *phase field crystal* method (PFC) [33, 34, 35]. This methodology describes the evolution of the atomic density of a system according to dissipative dynamics driven by free energy minimization. In the PFC approach the free energy functional of a solid phase is minimized when the density field is periodic. As discussed in prior publications [33, 34, 35] the periodic nature of the density field naturally gives rise to elastic effects, multiple crystal orientations and the nucleation and motion of dislocations. While these physical features are included in other atomistic approaches (such as molecular dynamics) a significant advantage of the PFC method is that, by construction, it is restricted to operate on diffusive time scales not on the prohibitively small time scales associated with atomic lattice vibrations. A similar approach has also been recently proposed by Jin and Khachatryan [36]. In the case of pure materials the PFC approach has been shown [33, 34] to model many phenomena dominated by atomic scale elastic and plastic deformation effects. These include grain boundary interactions, epitaxial growth and the yield strength of nano-crystals.

The original PFC model is among the simplest mathematical descriptions that can self-consistently combine

the physics of atomic-scale elasto-plasticity with the diffusive dynamics of phase transformations and microstructure formation. Nevertheless, analogously to traditional phase field modeling of solidification, further work is required to fully exploit the methodology. More specifically it is important to be able to generalize the method to more complex situations (binary alloys, faster dynamics, different crystal structures, etc.), to develop more efficient numerical techniques and to make a direct connection of the parameters of the model to experimental systems. Several innovations toward this goal have already been developed. Goldenfeld *et al.* [37, 40] have recently derived amplitude equations for the PFC model which are amenable to adaptive mesh refinement schemes. This work has the potential to enable simulations of mesoscopic phenomena ( $\mu\text{m} \rightarrow \text{mm}$ ) that are resolved down to the atomic scale and incorporate all the physics discussed above. Another recent advance is the inclusion of higher order time derivatives in the dynamics to simulate “instantaneous” elastic relaxation [41]. This extension is important for modeling complex stress propagation and externally imposed strains. Very recently, Wu *et al.* [51] fitted the PFC parameters to experimental data in iron and were able to show that the PFC model gives an accurate description of the anisotropy of the surface tension. In addition to this work Wu and Karma have also developed a simple and elegant scheme to extend the method to other crystal symmetries (i.e., FCC in three dimensions).

The purpose of this paper is to link the formalism of density function theory (DFT) of freezing, as formulated by Ramakrishnan and Yussouff [52] (and also reviewed by many other authors, such as Singh [53]) with the phase field crystal (PFC) method and to exploit this connection to develop a phase field crystal model for binary alloys. The organization of the paper and a summary of the remaining sections is as follows.

In Section IIA the density functional theory of freezing of pure and binary systems is briefly outlined. In this approach the free energy functional is written in terms of the time averaged atomic density field  $\rho$  ( $\rho_A$  and  $\rho_B$  in binary systems) and expanded around a liquid reference state existing along the liquid/solid coexistence line. Formally the expansion contains the  $n$ -point correlation functions of the liquid state. In this work the series expansion of the free energy is truncated at the 2-point correlation function,  $C(\vec{r}_1, \vec{r}_2)$ .

Within this framework it is shown in Section IIIA that the PFC model for a pure material can be recovered from DFT if  $C(\vec{r}_1, \vec{r}_2)$  is parameterized by three constants related to the liquid and solid state compressibilities and the lattice constant. The parameters of the PFC model can thus be directly related to the physical constants that enter the DFT of freezing and the PFC model can be viewed as a simplified form of DFT. In Section IIIB a binary system is considered. Similar to the case of pure materials the free energy expansion of a binary alloy will be truncated at the 2-point correlation functions which

are then characterized by three parameters. At this level of simplification it is shown that the “regular” solution model used in materials physics for alloys can be obtained directly from density functional theory. It is shown that the phenomenological nearest neighbour bond energies that enter the “regular” solution model are equal to the compressibilities that enter density functional theory. This section also provides insight into the concentration dependence of various properties of the crystalline phase of a binary alloy such as the lattice constant, effective mobilities and elastic constants.

In Section III C a simplified version of the binary alloy free energy is derived. This is done in order to provide a mathematically simpler model that can more transparently illustrate the use of the PFC formalism in simultaneously modeling diverse processes such as solidification, grain growth, defect nucleation, phase segregation and elastic and plastic deformation. This section also shows that the free energy of the simplified alloy PFC model reproduces two common phase diagrams associated with typical binary alloys in materials science.

In Section IV dynamical equations of motion that govern the evolution of the solute concentration and density field of the binary alloy are derived. Finally in Section V the simplified binary alloy model is used to simulate several important applications involving the interplay of phase transformation kinetics and elastic and plastic effects. This includes solidification, epitaxial growth and spinodal decomposition. Some of the more tedious calculations are relegated to the Appendices.

## II. DENSITY FUNCTIONAL THEORY OF FREEZING

In this section free energy functionals of pure and binary systems as derived from the density functional theory of freezing are presented. A derivation of the functional for a pure material is outlined in the Appendix B. For a more rigorous treatment the reader is referred to the work of Ramakrishnan and Yussouff [52] and numerous other very closely related review articles by Singh [53], Evans [54] and references therein.

### A. Single Component System

In density functional theory the emergence of an ordered phase during solidification can be viewed as a transition to a phase in which the atomic number density,  $\rho(\vec{r})$ , is highly non-homogenous and possesses the spatial symmetries of the crystal [53]. This approach implicitly integrates out phonon modes in favour of a statistical view of the ordered phase that changes on diffusive time scales. The free energy functional of a system is expressed in terms of  $\rho$  and constitutes the starting point of the PFC model.

In this work the free energy functional, denoted  $\mathcal{F}[\rho]$ , is expanded functionally about a density,  $\rho = \rho_l$ , corresponding to a liquid state lying on the liquidus line of the solid-liquid coexistence phase diagram of a pure material as shown in Fig. (1a). The expansion is performed in powers of  $\delta\rho \equiv \rho - \rho_l$ .

As shown by other others and outlined in Appendix B the free energy density can be written as

$$\begin{aligned} \frac{\mathcal{F}_c}{k_B T} &= \int d\vec{x} \left[ \rho(\vec{r}) \ln \left( \frac{\rho(\vec{r})}{\rho_l} \right) - \delta\rho(\vec{r}) \right] \\ &- \frac{1}{2} \int d\vec{r}_1 d\vec{r}_2 \delta\rho(\vec{r}_1) C_2(\vec{r}_1, \vec{r}_2) \delta\rho(\vec{r}_2) + \\ &- \frac{1}{6} \int d\vec{r}_1 d\vec{r}_2 d\vec{r}_3 \delta\rho(\vec{r}_1) C_3(\vec{r}_1, \vec{r}_2, \vec{r}_3) \delta\rho(\vec{r}_2) \delta\rho(\vec{r}_3) \\ &+ \dots \end{aligned} \quad (1)$$

where  $\mathcal{F}_c$  is the free energy corresponding to the density  $\rho(\vec{r})$  minus that at the constant density  $\rho_l$ . The function,  $C_2$  is the two point direct correlation function of an isotropic fluid. It is usually denoted  $C_{ij} \equiv C_2(r_{12})$  and satisfies  $r_{12} \equiv |\vec{r}_1 - \vec{r}_2|$ . The function  $C_3$  is the three point correlation function, etc.. Formally the correlation functions are defined by

$$\begin{aligned} C_1(\vec{r}) &\equiv \frac{\delta\Phi[\rho(\vec{r})]}{\delta\rho(\vec{r})} \\ C_2(\vec{r}_1, \vec{r}_2) &\equiv \frac{\delta^2\Phi}{\delta\rho(\vec{r}_1)\delta\rho(\vec{r}_2)} \\ C_3(\vec{r}_1, \vec{r}_2, \vec{r}_3) &\equiv \frac{\delta^3\Phi}{\delta\rho(\vec{r}_3)\delta\rho(\vec{r}_1)\delta\rho(\vec{r}_2)} \\ &\dots \end{aligned} \quad (2)$$

where  $\Phi[\rho]$  represents the total potential energy of interactions between the particles in the material. The proof that  $\Phi$  is a functional of  $\rho$  is shown rigorously in Evans [54].

### B. Multi-Component System

For an alloy involving one or more components the free energy functional of a pure material in Eq. (1) is extended to the form

$$\begin{aligned} \frac{\mathcal{F}_c}{k_B T} &= \sum_i \int d\vec{r} \left[ \rho_i(\vec{r}) \ln \left( \rho_i(\vec{r}) / \rho_l^i \right) - \delta\rho_i(\vec{r}) \right] \\ &- \frac{1}{2} \sum_{i,j} \int d\vec{r}_1 d\vec{r}_2 \delta\rho_i(\vec{r}_1) C_{ij}(\vec{r}_1, \vec{r}_2) \delta\rho_j(\vec{r}_2) + \dots \end{aligned} \quad (3)$$

where the sums are over the elements in the alloy,  $\delta\rho_i \equiv \rho_i - \rho_l^i$ ,  $\rho_l^i$  is the value of the number density of component  $i$  on the liquid side of the liquid/solid coexistence line. The function  $C_{ij}$  is the two point direct correlation function of between components  $i$  and  $j$  in an isotropic

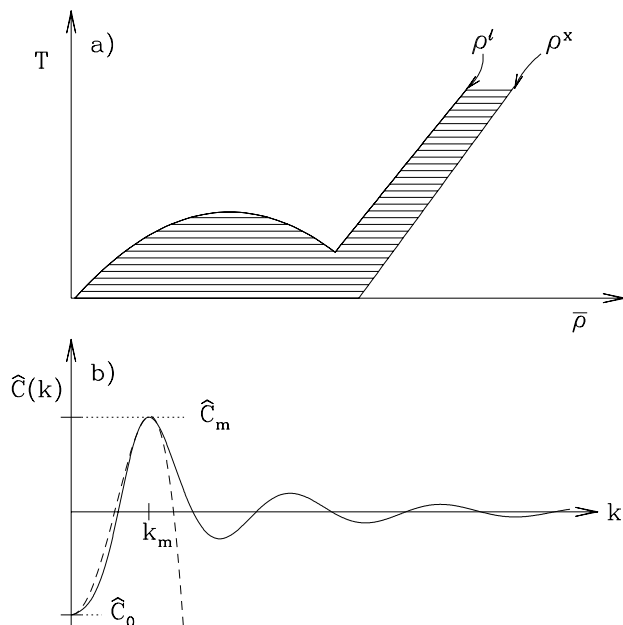


FIG. 1: (a) Sample phase diagram. In this figure the shaded area corresponds to a coexistence region. In the calculations presented in this paper the correlation functions are taken from points along the liquidus line at density  $\rho^\ell$ . (b) In this figure a ‘typical’ liquid state two-point direct correlation function is sketched. The dashed line represents the approximation used in most of the manuscript.

fluid. As in the case of a pure materials it will be assumed that  $C_{ij} \equiv C_{ij}(r_{12})$ , where  $r_{12} \equiv |\vec{r}_1 - \vec{r}_2|$ . The next term in the expansion of Eq. (3) contains the three point correlation, the next after that, the four point, etc.. In this paper only two point correlations will be considered, but it must be stressed that these higher order correlations maybe crucial for some systems, such as Si. Before considering the properties of the binary alloy free energy in detail it is instructive to first study the properties of a pure system and show the connection between this formalism and the original phase field crystal model.

### III. ANALYSIS OF FREE ENERGY FUNCTIONALS

#### A. Pure Materials

In this section the free energy functional of a single component alloy is considered in the limit that the series

given in Eq. (1) can be truncated at  $C_2$ , i.e.,

$$\begin{aligned} \mathcal{F}/k_B T &= \int d\vec{r} [\rho \ln(\rho/\rho_\ell) - \delta\rho] \\ &- (1/2) \int d\vec{r} d\vec{r}' \delta\rho C(\vec{r}, \vec{r}') \delta\rho' \end{aligned} \quad (4)$$

where, for convenience, the subscript ‘2’ has been dropped from the two-point correlation function as has the subscript  $c$  from  $\mathcal{F}_c$ . To understand the basic features of this free energy functional it is useful to expand  $\mathcal{F}$  in the dimensionless deviation of the density  $\rho$  from its average,  $\bar{\rho}$ , using the re-scaled density

$$n \equiv (\rho - \bar{\rho})/\bar{\rho}. \quad (5)$$

Expanding  $\mathcal{F}$  in powers of  $n$  gives,

$$\frac{\Delta\mathcal{F}}{\bar{\rho} k_B T} = \int d\vec{r} \left[ n \frac{1 - \bar{\rho} C}{2} n - \frac{n^3}{6} + \frac{n^4}{12} - \dots \right], \quad (6)$$

where  $\Delta\mathcal{F} \equiv \mathcal{F} - \mathcal{F}_o$  and  $\mathcal{F}_o$  is the the free energy functional at constant density (i.e.,  $\rho = \bar{\rho}$ ). For simplicity  $C$  is an operator defined such that  $n C n \equiv \int d\vec{r}' n(\vec{r}) C(|\vec{r} - \vec{r}'|) n(\vec{r}')$ . Terms that are linearly proportional to  $n$  in the above integral are identically zero by definition.

To gain insight into the properties of the free energy functional in Eq. (6) it is useful to expand the two point correlation function in a fourier series, i.e.,

$$\hat{C} = \hat{C}_0 + \hat{C}_2 k^2 + \hat{C}_4 k^4 + \dots \quad (7)$$

(in real space this corresponds to  $C = (\hat{C}_0 - \hat{C}_2 \nabla^2 + \hat{C}_4 \nabla^4 - \dots) \delta(\vec{r} - \vec{r}')$ , where the gradients are with respect to  $\vec{r}''$ ). The function  $\hat{C}$  is sketched for a typical liquid in Fig. (1b). In what follows only terms up to  $k^4$  will be retained. In this manner the properties of the material are parameterized by the three variable,  $\hat{C}_0$ ,  $\hat{C}_2$  and  $\hat{C}_4$ . To fit the first peak in  $\hat{C}$ ,  $\hat{C}_0$ ,  $\hat{C}_2$  and  $\hat{C}_4$  must be negative, positive and negative, respectively. These variables are related to three basic properties of the material, the liquid phase isothermal compressibility ( $\sim (1 - \bar{\rho} \hat{C}_0)$ ), the bulk modulus of the crystal ( $\sim \bar{\rho} \hat{C}_2^2 / |\hat{C}_4|$ ) and lattice constant ( $\sim (\hat{C}_2 / |\hat{C}_4|)^{1/2}$ ). In other words the  $k = 0$  term is related to the liquid phase isothermal compressibility, the height of the first peak ( $\hat{C}_m$  in Fig. (1b)) is related to the bulk modulus of the crystalline phase and the position of the first peak determines the lattice constant.

It is important to note that at this level of simplification the material is only defined by three quantities which may not be enough to fully parameterize any given material. For example this simple three parameter model always predicts triangular symmetry in two dimensions and BCC symmetry in three dimensions. Other crystal symmetries can be obtained by using more complicated 2-point correlation functions [51] or by including higher order correlation functions.

In two dimensions  $\mathcal{F}$  is minimized by a triangular lattice that can be represented to lowest order by a one-mode approximation as

$$n = A \left( \frac{1}{2} \cos \left( \frac{2qy}{\sqrt{3}} \right) - \cos(qx) \cos \left( \frac{qy}{\sqrt{3}} \right) \right). \quad (8)$$

Substituting Eq. (8) into Eq. (6) gives,

$$\begin{aligned} \Delta F = & \frac{3}{16}(1 - \bar{\rho} \hat{C}_0) A^2 - \frac{1}{32} A^3 + \frac{15}{512} A^4 - \dots \\ & - \bar{\rho} \left( \frac{1}{4} \hat{C}_2 q^2 + \frac{1}{3} \hat{C}_4 q^4 + \dots \right) A^2 \end{aligned} \quad (9)$$

where  $\Delta F \equiv \Delta \mathcal{F} / (\bar{\rho} k_B T S)$  and  $S$  is the area of a unit cell. Minimizing  $\Delta F$  with respect to  $q$  gives the equilibrium wavevector,  $q_{eq}$ , which is

$$q_{eq} = \sqrt{3 \hat{C}_2 / (8 |\hat{C}_4|)}. \quad (10)$$

or in terms of the equilibrium lattice constant  $a_{eq} = 2\pi/q_{eq}$ . When  $q = q_{eq}$ ,  $\Delta \mathcal{F}$  becomes

$$\Delta F = \frac{3}{16} \Delta B A^2 - \frac{1}{32} A^3 + \frac{15}{512} A^4 + \dots, \quad (11)$$

where  $\Delta B \equiv B^\ell - B^s$ ,  $B^\ell \equiv 1 - \bar{\rho} \hat{C}_0$  and  $B^s \equiv \bar{\rho} (\hat{C}_2)^2 / (4 |\hat{C}_4|)$ . The parameter  $B^\ell$  is the dimensionless bulk modulus of the liquid state (i.e.,  $B^\ell = \kappa / (\bar{\rho} k_B T)$ , where  $\kappa$  is the bulk modulus of a liquid). The parameter  $B^s$  is proportional to the bulk modulus in the crystalline phase.

Equation (11) indicates that the liquid state is linearly unstable to the formation of the crystalline phase when  $\Delta B < 0$ . This instability arises from a competition between the elastic energy stored in the liquid and crystalline phases. It is interesting to note that  $\Delta B$  can also be written,

$$\Delta B = (\bar{\rho}_s - \bar{\rho}) / \bar{\rho}_s \quad (12)$$

where  $\bar{\rho}_s = 1/\hat{C}_m$  and  $\hat{C}_m$  is the height of the first peak of  $\hat{C}$  as shown in Fig. (1). Written in this form  $\bar{\rho}_s$  can be thought of as defining the effective spinodal density, i.e., the average density at which the liquid becomes linearly unstable to crystallization.

Unfortunately it is difficult to obtain the equilibrium state (i.e., by solving  $d\Delta F/dA = 0$ ) without truncating the infinite series in Eq. (11). If only terms to order  $A^4$  are retained an analytic approximation can be obtained for the amplitude ( $A_{min}$ ) that minimizes  $\mathcal{F}$ . In this approximation the solution is

$$A_{min} = 2 \left( 1 + \sqrt{20 \bar{\rho} / \bar{\rho}_s - 19} \right) / 5. \quad (13)$$

Thus solutions for a crystalline state exist when  $\bar{\rho} > 19/20 \bar{\rho}_s$ .

It is also straightforward to calculate the change in energy of the crystalline state upon deformation (i.e., bulk,

shear or deviatoric). Details of similar calculations are given in previous publications [33, 34]. The result of these two-dimensional calculations gives the dimensionless bulk modulus,  $B_c$ , of the crystalline phase, i.e.,

$$B_c = \frac{3}{32} \bar{\rho} \frac{(\hat{C}_2)^2}{|\hat{C}_4|} A_{min}^2 = \frac{3}{8} B^s A_{min}^2. \quad (14)$$

In other words the parameter  $B^s$  controls the bulk modulus of the crystalline phase.

These calculations can be easily extended to three dimensions. As discussed previously this particular approximation for  $\hat{C}$  leads to a BCC crystal in three dimensions which can be represented in a one mode approximation as,

$$\begin{aligned} n = & A \left( \cos(qx) \cos(qy) + \cos(qx) \cos(qz) \right. \\ & \left. + \cos(qy) \cos(qz) \right). \end{aligned} \quad (15)$$

Substituting this functional form into the free energy and minimizing with respect to  $q$  gives,

$$q_{eq}^{3d} = \sqrt{\hat{C}_2 / |\hat{C}_4|}, \quad (16)$$

and the free energy functional at this  $q$  is,

$$\Delta F^{3d} = \frac{3}{8} \Delta B A^2 - \frac{1}{8} A^3 + \frac{45}{256} A^4 + \dots. \quad (17)$$

Thus in this instance the 'spinodal' occurs at the same density as in the two dimensional case. If the series is truncated at  $A^4$  the amplitude that minimizes the free energy is then

$$A_{min}^{3d} = 4 \left( 1 + \sqrt{15 \bar{\rho} / \bar{\rho}_s - 14} \right) / 15. \quad (18)$$

Thus in this approximations crystalline (BCC) solutions only exist if  $\bar{\rho} > 14 \bar{\rho}_s$ . In addition the elastic constants can also be calculated in 3D in the usual manner. For example the dimensionless bulk modulus of the crystalline state is given by;

$$B_c^{3d} = 3 B^s (A_{min}^{3d})^2. \quad (19)$$

This calculation gives the basic functional dependence of the (dimensionless) bulk modulus on  $B^s$  and the amplitude. For a more accurate calculation higher order fourier components and more terms in the powers series in  $n$  should be retained.

Finally it is useful to consider fixing the density and varying the temperature. If the liquidus and solidus lines are roughly linear then,  $\bar{\rho}_s$  can be approximated by a linear function of temperature. In the sample phase diagram shown in Fig. (1a) the liquidus and solidus lines are roughly parallel and it is likely that the spinodal is also roughly parallel to these lines. In this case  $\Delta B$  can be written,

$$\Delta B = \alpha \Delta T \quad (20)$$

where  $\Delta T \equiv (T - T_s) / T_s$ ,  $T_s$  is the spinodal temperature and  $\alpha \equiv (T_s / \bar{\rho}_s) (\partial \bar{\rho}_s / \partial T_s)$ , evaluated at  $\rho = \bar{\rho}$ .

## B. Binary Alloys

For a binary alloy made up of ‘A’ and ‘B’ atoms the free energy functional can be written to lowest order in terms of the direct correlation functions as,

$$\begin{aligned} \frac{\mathcal{F}}{k_B T} = & \int d\vec{r} \left[ \rho_A \ln \left( \frac{\rho_A}{\rho_\ell^A} \right) - \delta\rho_A + \rho_B \ln \left( \frac{\rho_B}{\rho_\ell^B} \right) - \delta\rho_B \right] \\ & - \frac{1}{2} \int d\vec{r}_1 d\vec{r}_2 \left[ \delta\rho_A(\vec{r}_1) C_{AA}(\vec{r}_1, \vec{r}_2) \delta\rho_A(\vec{r}_2) \right. \\ & \quad + \delta\rho_B(\vec{r}_1) C_{BB}(\vec{r}_1, \vec{r}_2) \delta\rho_B(\vec{r}_2) \\ & \quad \left. + 2\delta\rho_A(\vec{r}_1) C_{AB}(\vec{r}_1, \vec{r}_2) \delta\rho_B(\vec{r}_2) \right] \quad (21) \end{aligned}$$

where  $\delta\rho_A \equiv \rho_A - \rho_\ell^A$  and  $\delta\rho_B \equiv \rho_B - \rho_\ell^B$ . It is assumed here that all two point correlation functions are isotropic, i.e.,  $C_{ij}(\vec{r}_1, \vec{r}_2) = C_{ij}(|\vec{r}_1 - \vec{r}_2|)$ .

In order to make a connection between the alloy free energy and standard phase field models it is useful to define the total number density,  $\rho \equiv \rho_A + \rho_B$  and a local concentration field  $c \equiv \rho_A/\rho$ . In terms of these fields the atomic densities can be written,  $\rho_A = c\rho$  and  $\rho_B = \rho(1-c)$ . Furthermore it is useful to define  $\rho = \rho_l + \delta\rho$  where  $\rho_l \equiv \rho_l^A + \rho_l^B$  and  $\delta c = 1/2 - c$ . Substituting these definitions into Eq. (21) gives,

$$\begin{aligned} \frac{\mathcal{F}}{k_B T} = & \int d\vec{r} \left[ \rho \ln(\rho/\rho_\ell) - \delta\rho + \right. \\ & \quad - \frac{1}{2} \delta\rho \{ c C_{AA} + (1-c) C_{BB} \} \delta\rho \\ & \quad + \rho \{ c \ln(c) + (1-c) \ln(1-c) \} \\ & \quad \left. + \rho c \Delta C (1-c)\rho + \beta \delta c + F_o \right] \quad (22) \end{aligned}$$

where

$$\begin{aligned} \Delta C & \equiv (C_{AA} + C_{BB})/2 - C_{AB}, \\ \beta & \equiv \frac{\rho_l}{2} (C_{AA} - C_{BB})(\rho + \rho_l) + \rho \ln \left( \frac{\rho_\ell^B}{\rho_\ell^A} \right) \quad (23) \end{aligned}$$

and

$$\begin{aligned} F_o & \equiv \rho \ln \left( \frac{\rho_\ell}{\sqrt{\rho_\ell^A \rho_\ell^B}} \right) - \frac{C_{AA}}{2} \left( (\rho_\ell^A)^2 + \frac{\rho_l}{2} (\rho_l + \rho) \right) \\ & \quad - \frac{C_{BB}}{2} \left( (\rho_\ell^B)^2 + \frac{\rho_l}{2} (\rho_l + \rho) \right). \quad (24) \end{aligned}$$

To illustrate the properties of the model in Eq. (22) it is useful to consider two limiting cases, a liquid phase at constant density and a crystalline phase at constant concentration. These calculations are presented in following two sub-sections.

### 1. Liquid phase properties

In the liquid phase  $\rho$  is constant on average and in the mean field limit can be replaced by  $\rho = \bar{\rho}$ . To simplicity

calculations, the case  $\rho = \bar{\rho} \approx \rho_\ell$  (or  $\delta\rho \approx 0$ ) will now be considered. As in the previous section it is useful to expand the direct correlation functions in Fourier space, i.e.,

$$\hat{C}_{ij} = \hat{C}_0^{ij} + \hat{C}_2^{ij} k^2 + \hat{C}_4^{ij} k^4 + \dots \quad (25)$$

where the subscript  $i$  and  $j$  refer to a particular element. Substituting the real-space counterpart of the Fourier expansion for  $\hat{C}_{ij}$  (to order  $k^2$ ) into Eq. (22) gives,

$$\begin{aligned} \frac{\mathcal{F}_C}{\bar{\rho} k_B T} = & \int d\vec{r} \left[ c \ln(c) + (1-c) \ln(1-c) \right. \\ & \quad \left. + \frac{\bar{\rho} \Delta \hat{C}_0}{2} c(1-c) + \gamma^\ell \delta c + \frac{\bar{\rho} \Delta \hat{C}_2}{2} |\nabla c|^2 \right] \quad (26) \end{aligned}$$

where  $\mathcal{F}_C$  is the total free energy minus a constant that that depends only on  $\bar{\rho}$ ,  $\rho_\ell^A$  and  $\rho_\ell^B$ ,

$$\gamma^\ell \equiv (B_\ell^{BB} - B_\ell^{AA}) + \bar{\rho} \ln(\rho_\ell^B/\rho_\ell^A), \quad (27)$$

$$\Delta \hat{C}_n \equiv \hat{C}_n^{AA} + \hat{C}_n^{BB} - 2\hat{C}_n^{AB}. \quad (28)$$

and  $B_\ell^{ij} = 1 - \bar{\rho} \hat{C}_0^{ij}$  is the dimensionless bulk compressibility. Equation (26) is the regular solution model of a binary alloy.

The coefficient of  $c(1-c)$  in Eq. (26) is given by

$$\bar{\rho} \Delta \hat{C}_0 = 2B_\ell^{AB} - B_\ell^{AA} - B_\ell^{BB}. \quad (29)$$

This result shows that in the liquid state the ‘interaction’ energies that enter regular solution free energies are simply the compressibilities (or the elastic energy) associated with the atomic species. The  $\gamma^\ell$  term is also quite interesting as it is responsible for asymmetries in the phase diagram. Thus Eq. (27) implies that asymmetries can arise from either different compressibilities or different densities.

Expanding Eq. (26) around  $c = 1/2$  gives,

$$\frac{\Delta \mathcal{F}_C}{\bar{\rho} k_B T} = \int d\vec{r} \left[ \frac{r^\ell}{2} \delta c^2 + \frac{u}{4} \delta c^4 + \gamma^\ell \delta c + \frac{K}{2} |\nabla c|^2 \right] \quad (30)$$

where,  $\Delta \mathcal{F}_C \equiv \mathcal{F}_C - \bar{\rho} k_B T \int d\vec{r} (\bar{\rho} \Delta \hat{C}_0 / 8 - \ln(2))$ ,  $u \equiv 16/3$ ,  $r^\ell \equiv (4 - \bar{\rho} \Delta \hat{C}_0)$  and  $K = \bar{\rho} \Delta \hat{C}_2$ . The parameter  $r^\ell$  is related only to the  $k = 0$  part of the two-point correlation function and can be written,

$$r^\ell = 4 + (B_\ell^{AA} + B_\ell^{BB} - 2B_\ell^{AB}). \quad (31)$$

This result implies that the instability to phase segregation in the fluid is a competition between entropy (4) and the elastic energy of a mixed fluid ( $2B_\ell^{AB}$ ) with the elastic energy associated with a phase separated fluid ( $B_\ell^{AA} + B_\ell^{BB}$ ). Replacing the dimensionless bulk moduli with the dimensional version (i.e.,  $B = \kappa/k_B T$ ), gives the critical point (i.e.  $r^\ell = 0$ ) as

$$T_C^\ell = (2\kappa_{AB} - \kappa_{BB} - \kappa_{AA}) / (4k_B). \quad (32)$$

where  $\kappa$  is the dimensional bulk modulus.

The properties of the crystalline phase are more complicated but at the simplest level the only real difference is that the elastic energy associated with the crystalline state must be incorporated. This is discussed in the next section.

## 2. Crystalline phase properties

To illustrate the properties of the crystalline state, the case in which the concentration field is a constant is considered. In this limit the free energy functional given in Eq. (22) can be written in the form

$$\frac{\mathcal{F}}{k_B T} \equiv \int d\vec{r} \left[ \rho \ln \left( \frac{\rho}{\rho_\ell} \right) - \delta\rho - \frac{1}{2} \delta\rho \bar{C} \delta\rho + G \right] \quad (33)$$

where  $G$  is a function of the concentration  $c$  and  $\rho_l$  and couples only linearly to  $\delta\rho$ . The operator  $\bar{C}$  can be written as

$$\bar{C} \equiv c^2 C_{AA} + (1-c)^2 C_{BB} + 2c(1-c) C_{AB}. \quad (34)$$

Thus in the limit that the concentration is constant this free energy functional is that of a pure material with an effective two point correlation function that is an average over the  $AA$ ,  $BB$  and  $AB$  interactions. In this limit the calculations presented in section III A can be repeated using the same approximations (i.e., expanding  $\rho$  around  $\rho_\ell$ , expanding  $\bar{C}$  to  $\nabla^4$  and using a one mode approximation for  $\delta\rho$ ) to obtain predictions for the concentration dependence of various quantities. For example the concentration dependence of the equilibrium wavevector (or lattice constant, Eq. (10)) and bulk modulus Eq. (14) can be obtained by substituting  $\hat{C}_n = c^2 \hat{C}_n^{AA} + (1-c)^2 \hat{C}_n^{BB} + 2c(1-c) \hat{C}_n^{AB}$ .

As a more specific example the equilibrium lattice constant can be expanded around  $c = 1/2$  to obtain in two or three dimensions,

$$a_{eq}(\delta c) = a_{eq}(0) (1 + \eta \delta c + \dots) \quad (35)$$

where  $\delta c = c - 1/2$  and  $\eta$  is the solute expansion coefficient given by,

$$\eta = (\delta \hat{C}_4 - \delta \hat{C}_2)/2 \quad (36)$$

where

$$\delta \hat{C}_n \equiv (\hat{C}_n^{AA} - \hat{C}_n^{BB})/\hat{C}_n^o \quad (37)$$

and  $\hat{C}_n^o \equiv \hat{C}_n(\delta c = 0) = (\hat{C}_n^{AA} + \hat{C}_n^{BB} + 2\hat{C}_n^{AB})/4$ .

This line of reasoning can also be used to understand the influence of alloy concentration on crystallization. Specifically, for the case of an alloy, the terms in Eq. (11) (with  $A$  replaced with  $A_{min}$ ) become functions of concentration, since  $\Delta B$  and  $A_{min}$  are concentration dependent. Here,  $\Delta B$  can be expanded around  $c = 1/2$ , i.e.,

$$\Delta B(\delta c) = \Delta B_0 + \Delta B_1 \delta c + \Delta B_2 \delta c^2 + \dots \quad (38)$$

where  $\Delta B_0 = B_0^l - B_0^s$ ,  $\Delta B_1 = B_1^l - B_1^s$  and  $\Delta B_2 = B_2^l - B_2^s$  are determined in the appendix. This would imply that in the crystalline phase the free energy has a term of the form,  $r^c(\delta c)^2$ , where

$$\begin{aligned} r^c &= r^\ell + \frac{3\Delta B_2}{8} A_{min}^2 \\ &= 4 - \bar{\rho} \Delta \hat{C}_0 (1 + 3A_{min}^2/8) - 3/8 B_2^s A_{min}^2, \end{aligned} \quad (39)$$

in two dimensions (in three dimensions the  $3/8$  factor is replaced with  $3/4$ ). This result indicates that crystallization (i.e., a non-zero  $A_{min}$ ) favours phase segregation, assuming  $\kappa_{AA} + \kappa_{BB} < 2\kappa_{AB}$ . For example, when  $B_2^s = 0$ , the critical temperature increases and can be written,

$$T_C^c = T_C^\ell (1 + 3A_{min}^2/8), \quad (40)$$

or  $T_C^c = T_C^\ell (1 + 3A_{min}^2/4)$  in three dimensions.

## C. Simple Binary Alloy Model

In this section a simple binary alloy model is proposed based on a simplification of the free energy in Eq. (22). The goal of this section is to develop a mathematically *simple* model that can be used to simultaneously model grain growth, solidification, phase segregation in the presence of elastic and plastic deformation. To simplify calculations it is convenient to first introduce the following dimensionless fields,

$$\begin{aligned} n_A &\equiv (\rho_A - \bar{\rho}_A)/\bar{\rho} \\ n_B &\equiv (\rho_B - \bar{\rho}_B)/\bar{\rho}. \end{aligned} \quad (41)$$

Also, it is convenient to expand in the following two fields,

$$\begin{aligned} n &= n_A + n_B \\ \delta N &= (n_B - n_A) + \frac{\bar{\rho}_B - \bar{\rho}_A}{\bar{\rho}}. \end{aligned} \quad (42)$$

The following calculations will use the field  $\delta N$  instead of  $\delta c$ . Expanding Eq. (22) around  $\delta N = 0$  and  $n = 0$  gives a free energy of the form

$$\begin{aligned} \frac{\mathcal{F}}{\bar{\rho} k_B T} &= \int d\vec{r} \left( \frac{n}{2} [B_\ell + B_s (2R^2 \nabla^2 + R^4 \nabla^4)] n \right. \\ &\quad + \frac{t}{3} n^3 + \frac{v}{4} n^4 + \gamma \delta N + \frac{w}{2} \delta N^2 + \frac{u}{4} \delta N^4 \\ &\quad \left. + \frac{L^2}{2} |\vec{\nabla} \delta N|^2 + \dots \right). \end{aligned} \quad (43)$$

Details of this free energy and explicit expressions for  $B^\ell$ ,  $B^s$  and  $R$  are given in Appendix C. For simplicity the calculations presented in this section are for a two dimensional system.

The transition from liquid to solid is intimately related to  $\Delta B = B^\ell - B^s$  as was the case for the pure material and can be written in terms of a temperature difference, i.e., Eq. (20). In addition some of the polynomial terms

in  $n$  and  $\delta N$  have been multiplied by variable coefficients even though they can be derived exactly as shown in Appendix C. For example the parameter  $v = 1/3$  recovers the exact form of the  $n^4$  term. This flexibility in the choice of coefficients was done to be able to match the parameter of the free energy with experimental materials parameters. As an example Wu and Karma [51] showed that adjusting the parameter  $v$  can be used to match the amplitude of fluctuations obtained in molecular dynamics simulations. With this fit they are able to accurately predict the anisotropy of the surface energy of a liquid/crystal interface in iron.

To facilitate the calculation of the lowest order phase diagram corresponding to Eq. (43) it is convenient to assume the concentration field  $\delta N$  varies significantly over length scales much larger than the atomic number density field  $n$ . As a result, the density field can be integrated out of the free energy functional. In this instance the one-mode approximation for  $n$ , i.e.,

$$n = A \left( \frac{1}{2} \cos \left( \frac{2qy}{\sqrt{3}} \right) - \cos(qx) \cos \left( \frac{qy}{\sqrt{(3)}} \right) \right). \quad (44)$$

will be used. Substituting Eq. (44) into Eq. (43) and minimizing with respect to  $q$  and  $A$  (recalling that  $\delta N$  is assumed constant over the scale that  $n$  varies) gives

$$q_{eq} = \sqrt{3}/(2R) \quad (45)$$

and

$$A_{min} = \frac{4}{15v} \left( t + \sqrt{t^2 - 15v\Delta B} \right). \quad (46)$$

The free energy that is minimized with respect to amplitude and lattice constant is then,

$$F_{sol} = \frac{w}{2}\delta N^2 + \frac{u}{4}\delta N^4 + \frac{3}{16}\Delta B A_{min}^2 - \frac{t}{16}A_{min}^3 + \frac{45v}{512}A_{min}^4. \quad (47)$$

For mathematical simplicity all further calculations will be limited to the approximations  $B^\ell = B_0^\ell + B_2^\ell(\delta N)^2$  and  $B^s = B_0^s$ . In this limit analytic expression can be obtained for a number of quantities and the free energy functional is still general enough to produce for example a eutectic phase diagram.

### 1. Solid-solid coexistence

Expanding  $F_{sol}$  around  $\delta N = 0$  gives,

$$F_{sol} = F_{sol}(0) + a\delta N^2/2 + b\delta N^4/4 + \dots \quad (48)$$

where

$$\begin{aligned} a &\equiv w + 3B_2^\ell (A_{min}^o)^2/8 \\ b &\equiv u - \frac{6(B_2^\ell)^2 A_{min}^o}{(15vA_{min}^o - 4t)} \end{aligned} \quad (49)$$

and  $A_{min}^o \equiv A_{min}(\delta N = 0)$  (which is thus a function of  $\Delta B_0$ ). This simple form can be used to calculate the solid/solid coexistence concentrations at low temperatures according to

$$\delta N_{coex} = \pm \sqrt{|a|/b}. \quad (50)$$

The critical temperature,  $\Delta B_0^C$  is determined by setting  $\delta N_{coex} = 0$  and solving for  $\Delta B_0$ , which gives,

$$\Delta B_0^c = \left( 15wv - 2t\sqrt{-6B_2^\ell w} \right) / (6B_2^\ell). \quad (51)$$

### 2. Solid-liquid coexistence

To obtain the liquid/solid coexistence lines the free energy of the liquid state must be compared to that of the solid. The mean field free energy of the liquid state is obtained by setting  $n = 0$  which gives,

$$F_{liq} = \frac{w}{2}\delta N^2 + \frac{u}{4}\delta N^4. \quad (52)$$

To obtain the solid-liquid coexistence lines it is useful to expand the free energy of the liquid and solid states around the value of  $\delta N$  at which the liquid and solid states have the same free energy, i.e., when  $F_{sol} = F_{liq}$ . This occurs when,

$$\delta N_{ls} = \pm \sqrt{(\Delta B_0^{ls} - \Delta B_o) / B_2^\ell}, \quad (53)$$

where  $\Delta B_o \equiv B_0^l - B_0^s$  and  $\Delta B_0^{ls} \equiv 8t^2/(135v)$  is the lowest value of  $\Delta B_0^{ls}$  at which a liquid can coexist with a solid. To complete the calculations,  $F_{sol}$  and  $F_{liq}$  are expanded around  $\delta N_{ls}$  to order  $(\delta N_{ls})^2$ , i.e.,

$$\begin{aligned} F_{liq} &= \mathcal{F}(\delta N_{ls}) + a_{liq}(\delta N - \delta N_{ls}) + b_{liq}(\delta N - \delta N_{ls})^2 \dots \\ F_{sol} &= \mathcal{F}(N_{ls}) + a_{sol}(\delta N - \delta N_{ls}) + b_{sol}(\delta N - \delta N_{ls})^2 \dots \end{aligned} \quad (54)$$

(note by definition  $F_{sol}(\delta N_{ls}) = F_{liq}(\delta N_{ls})$ ), where

$$\begin{aligned} a_{liq} &= (w + u\delta N_{ls}^2)\delta N_{ls} \\ a_{sol} &= a_{liq} + 32t^2 B_2^\ell \delta N_{ls} / (675v^2) \\ b_{liq} &= (w + 3u\delta N_{ls}^2)/2 \\ b_{sol} &= b_{liq} + \frac{6}{5v} B_2^\ell \left( \frac{4}{3} \Delta B_0 - \Delta B_0^{ls} \right) \end{aligned} \quad (55)$$

It is now straightforward to calculate the liquid/solid coexistence lines from Eq. (54) in terms of the parameters given above. The liquid/solidus lines are;

$$\begin{aligned} \delta N_{liq} &= \delta N_{ls} + \frac{1}{2} \left( \frac{a_{liq} - a_{sol}}{b_{sol} - b_{liq}} \right) \left( 1 - \sqrt{\frac{b_{sol}}{b_{liq}}} \right) \\ \delta N_{sol} &= \delta N_{ls} + \frac{1}{2} \left( \frac{a_{liq} - a_{sol}}{b_{sol} - b_{liq}} \right) \left( 1 - \sqrt{\frac{b_{liq}}{b_{sol}}} \right) \end{aligned} \quad (56)$$



for  $\delta N_{liq} > 0$ ,  $\delta N_{sol} > 0$  and similar results for  $\delta N_{liq} < 0$ ,  $\delta N_{sol} < 0$ , since  $F$  is a function of  $\delta N^2$  in this example. The calculations in this section and the previous section are reasonably accurate when  $\Delta B_0^{ls} > \Delta B_0^c$ , however in the opposite limit a eutectic phase diagram forms and the accuracy of the calculations decreases. This case will be discussed below.

### 3. Linear elastic constants

As shown in previous publications [33, 34], the elastic constants can be calculated analytically in a one mode approximation by considering changes in  $F$  as a function of strain. For the binary model similar calculations can be made in a constant  $\delta N$  approximation and give,

$$C_{11}/3 = C_{12} = C_{44} = \frac{3}{16} B^s (A_{min})^2. \quad (57)$$

(this calculation can be done for arbitrary dependence of  $B^s$  on  $\delta N$ ). As expected the elastic constants are directly proportional to the amplitude of the density fluctuations. This implies that the elastic constants decrease as the liquid solid transition is approached from the solid phase. This result implies both a temperature and concentration dependence through the dependence of  $A_{min}$  on  $\Delta B$ . In addition to this dependence (which might be considered as a 'thermodynamic' dependence) the magnitude of the elastic constants can be altered by the constant  $B^s$ .

### 4. Calculation of phase diagrams

To examine the validity of some of the approximations made in the previous section, numerical simulations were conducted to determine the properties of the solid and liquid equilibrium states. The simulations were performed over a range of  $\delta N$  values, three values of  $\Delta B_0$  and two values of  $w$ . The specific values of the constants that enter the model are given in the figure captions.

In Fig. (2) analytic predictions and numerical solutions are shown for the free energy,  $F$ , the lattice constant  $R$  and bulk modulus at three values of  $\Delta B_0$ , using the free energy functional given in Eq. (43). These figures indicate that the approximate solutions are quite accurate except for some deviations in the  $\delta N$  dependence of the bulk modulus. For the specific set of parameters used for these comparisons, the one-mode constant concentration approximation predicts no asymmetry in any quantity. However, it is clear from the numerical solutions that some symmetry does exist. Figure (3) shows the phase diagram corresponding to the parameters used in Fig. (2)

The same calculations presented in Figs. (2) and (3) were repeated using  $w = -0.04$  for which  $\Delta B_0^c > \Delta B_0^{ls}$ . In this case the agreement between the numerical results and the one-mode constant concentration calculations for the free energy, lattice constant and bulk modulus are

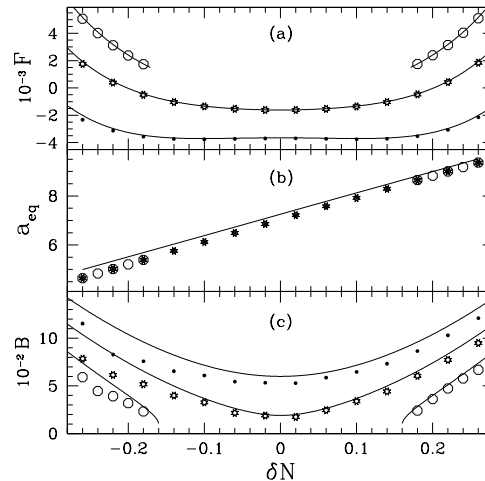


FIG. 2: Free energy (a), lattice constant (b) and bulk modulus (c) are plotted as a function of  $\delta N$  for three different values of  $\Delta B_0$ . In figure (a) the lines from top to bottom (and bottom to top in (c)) correspond to  $\Delta B_0 = 0.07$ ,  $0.02$  and  $-0.03$  respectively computed in the one-mode approximations. The solid, starred and open points correspond to  $\Delta B_0 = 0.07$ ,  $0.02$  and  $-0.03$  and were calculated directly by numerically minimizing the free energy functional given in Eq. (43). Other parameters used correspond  $B_0^s = 1.00$ ,  $B_1^l = 0$ ,  $B_2^l = -1.80$ ,  $t = 0.60$ ,  $v = 1.00$ ,  $w = 0.088$ ,  $u = 4.00$ ,  $L = 4.00$ ,  $Ro = 1.00$  and  $R_1 = 1.20$  (see Eq. C12 for definitions of  $R_o$  and  $R_1$ ).

similar to the  $w = 0.088$  case as shown in Fig. (4). The phase diagram corresponding to the parameters used in Fig. (4) is shown in Fig. (5). In this case, the analytic calculations (Eqns. (56) and (50)) for the coexistence lines breakdown at the eutectic point. Higher order terms in the in  $\delta N$  are needed to accurately predict the coexistence lines.

## IV. DYNAMICS

To simulate microstructure formation in binary alloys, dynamical equations of motions for the field  $\delta N$  and  $n$  need to be developed. The starting point is the full free energy in Eq. (21), written in terms of in terms of  $\rho_A$  and  $\rho_B$ , i.e.,  $\mathcal{F}(\rho_A, \rho_B)$ . The dynamics of  $\rho_A$  and  $\rho_B$  is assumed to be dissipative and driven by free energy

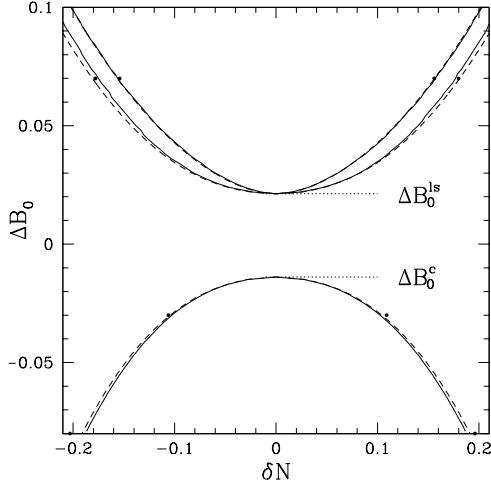


FIG. 3: Phase diagram of  $\Delta B_0$  Vs.  $\delta N$  for the parameters corresponding to the parameters of Fig. (2). The solid line is a numerical solution of the one mode approximation and the dashed lines are from Eq. (50) for the lower solid/solid coexistence lines and Eq. (56) for the upper liquid/solid coexistence lines. The solid points are from numerical solutions for the minimum free energy functional given in Eq. (43).

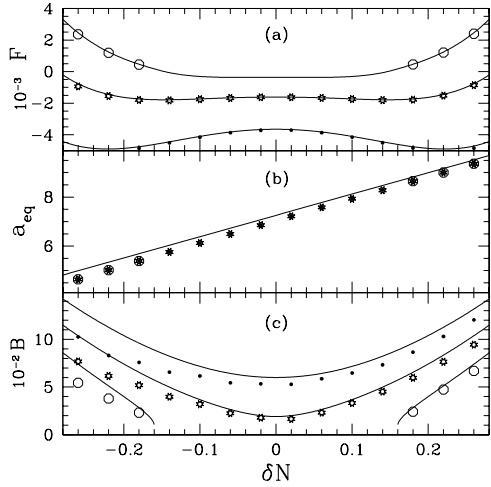


FIG. 4: This figure is identical to Fig. (2) with the exception that  $w = -0.04$ .

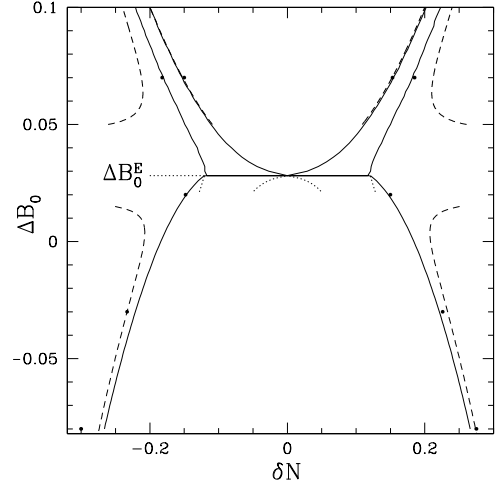


FIG. 5: Phase diagram of  $\Delta B_0$  Vs.  $\delta N$  for the same parameters as those used to generate Fig. (3), with the exception that  $w = -0.04$ . The dotted lines below the eutectic temperature,  $\Delta B_0^E \approx 0.028$ , correspond to metastable states.

minimization, i.e.,

$$\frac{\partial \rho_A}{\partial t} = \nabla \cdot \left( M_A(\rho_A, \rho_B) \nabla \frac{\delta \mathcal{F}}{\delta \rho_A} \right) \quad (58)$$

$$\frac{\partial \rho_B}{\partial t} = \nabla \cdot \left( M_B(\rho_A, \rho_B) \nabla \frac{\delta \mathcal{F}}{\delta \rho_B} \right) \quad (59)$$

where  $M_A$  and  $M_B$  are the mobilities of each density field. In general these mobilities depend on the density of each species. The free energy  $\mathcal{F}(\rho_A, \rho_B)$  can equivalently be defined in terms of  $n$  and  $\delta N$ . This allows the previous equations to be re-written as

$$\bar{\rho} \frac{\partial \rho_A}{\partial t} = (M_A \nabla^2 + \nabla \cdot M_A \nabla) \left( \frac{\delta \mathcal{F}}{\delta n} - \frac{\delta \mathcal{F}}{\delta(\delta N)} \right) \quad (60)$$

$$\bar{\rho} \frac{\partial \rho_B}{\partial t} = (M_B \nabla^2 + \nabla \cdot M_B \nabla) \left( \frac{\delta \mathcal{F}}{\delta n} + \frac{\delta \mathcal{F}}{\delta(\delta N)} \right). \quad (61)$$

Adding Eq.(60) and Eq.(61) and collecting terms gives the following equation for  $n$ ,

$$\begin{aligned} \frac{\partial n}{\partial t} = & \{ M_1 \nabla^2 + \nabla \cdot M_1 \cdot \nabla \} \frac{\delta \mathcal{F}}{\delta n} \\ & + \{ M_2 \nabla^2 + \nabla \cdot M_2 \cdot \nabla \} \frac{\delta \mathcal{F}}{\delta(\delta N)}. \end{aligned} \quad (62)$$

where  $M_1 \equiv (M_A + M_B)/\bar{\rho}^2$  and  $M_2 \equiv (M_B - M_A)/\bar{\rho}^2$ . Subtracting Eq.(60) from Eq.(61) similarly gives an equa-

tion for  $\delta N$ ,

$$\begin{aligned} \frac{\partial(\delta N)}{\partial t} &= \{M_2 \nabla^2 + \nabla M_2 \cdot \nabla\} \frac{\delta \mathcal{F}}{\delta n} \\ &+ \{M_1 \nabla^2 + \nabla M_1 \cdot \nabla\} \frac{\delta \mathcal{F}}{\delta(\delta N)}. \end{aligned} \quad (63)$$

Equations (62) and (63) can be cast into the more illuminating form

$$\frac{\partial n}{\partial t} = \vec{\nabla} \cdot \left\{ M_1 \vec{\nabla} \frac{\delta \mathcal{F}}{\delta n} \right\} + \vec{\nabla} \cdot \left\{ M_2 \vec{\nabla} \frac{\delta \mathcal{F}}{\delta(\delta N)} \right\} \quad (64)$$

$$\frac{\partial(\delta N)}{\partial t} = \vec{\nabla} \cdot \left\{ M_2 \vec{\nabla} \frac{\delta \mathcal{F}}{\delta n} \right\} + \vec{\nabla} \cdot \left\{ M_1 \vec{\nabla} \frac{\delta \mathcal{F}}{\delta(\delta N)} \right\}. \quad (65)$$

Equations (64) and (65) couple the dynamics of the fields  $\delta N$  and  $n$  through a symmetric mobility tensor. The dependence of the mobilities  $M_A$  and  $M_B$  will in general depend on local crystal density and the local relative concentration of species  $A$  to  $B$ .

For the case of substitutional diffusion between species  $A$  and  $B$ ,  $M_A \approx M_B \equiv M$ . In this limit the dynamics of  $n$  and  $\delta N$  decouple. Moreover if it is further assumed that the mobility is a constant, Eqs. (64) and (65) become

$$\frac{\partial n}{\partial t} = M_e \nabla^2 \frac{\delta \mathcal{F}}{\delta n} \quad (66)$$

$$\frac{\partial(\delta N)}{\partial t} = M_e \nabla^2 \frac{\delta \mathcal{F}}{\delta(\delta N)} \quad (67)$$

where the effective mobility  $M_e \equiv 2M/\bar{\rho}^2$ . In the applications using Eqs. (66) and (67) in the following sections, the dynamics of  $n$  and  $\delta N$  are simulated with time rescaled by  $t \rightarrow \bar{t} \equiv 2Mt/\bar{\rho}^2$ .

To illustrate the dynamics described by Eqs. (66), (67) and (43), a simulation of heterogenous eutectic crystallization from a supercooled homogenous liquid was performed. The results of this simulation are shown in Fig. (6). This figure shows the density ( $n$ ), the density difference ( $\delta N$ ) and the local energy density at three time steps in the solidification process. These figures show liquid/crystal interfaces, grain boundaries, phase segregation, dislocations and multiple crystal orientations all in a single numerical simulation of the simple binary alloy PFC model. In this simulation a simple Euler algorithm was used for the time derivative and the spherical Laplacian approximation introduced was used (see Appendix A). The grid size was  $\Delta x = 1.1$  and the time step was  $\Delta t = 0.05$ . Unless otherwise specified all simulations to follow use the same algorithm, grid size and time step.

## V. APPLICATIONS

This section applies the simplified phase field crystal model derived in Section III C, coupled to the dynamical equations of motion derived in Section IV, to the

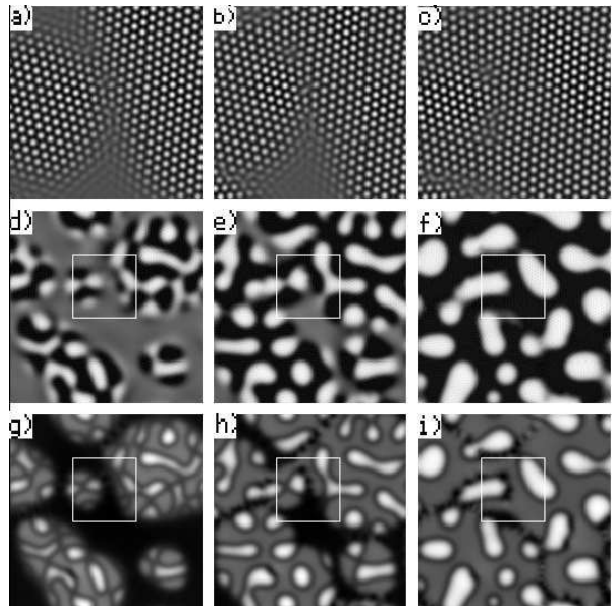


FIG. 6: The grey scales in the figure correspond to density ( $n$ ), concentration ( $\delta N$ ) and the local energy density in frames (a,b,c), (d,e,f) and (g,h,i) respectively. The area enclosed by white boxes is area shown in figures (a,b,c). The parameters in this simulation are the same as Fig. (5) except  $L = 1.20$  and  $R_1/R_0 = 1/4$  at  $\delta N = 0$  and  $\Delta B_o = 0.02$ . Figures (a,d,g), (b,e,h) and (c,f,i) correspond to times  $t = 6600, 16200, 49900$ , respectively.

study of elastic and plastic effects in phase transformations. The first application demonstrates how the PFC alloy model can be used to simulate eutectic and dendritic microstructures. That is followed by a discussion of the effects of compressive and tensile stresses in epitaxial growth. Finally, simulations demonstrating the role of dislocations in Spinodal decomposition are presented.

### A. Eutectic and Dendritic Solidification

One of the most important applications of the alloy phase field crystal model is the study of solidification microstructures. These play a prominent role in numerous applications such as commercial casting. Traditional phase field models of solidification are typically unable to self-consistently combine bulk elastic and plastic effects with phase transformation kinetics, multiple crystal orientations and surface tension anisotropy. While some of these effects have been included in previous approaches (e.g. surface tension anisotropy) they are usually introduced phenomenologically. In the PFC formalism, these features arise naturally from density functional theory.

To illustrate solidification microstructure formation using the PFC formalism, two simulations were conducted

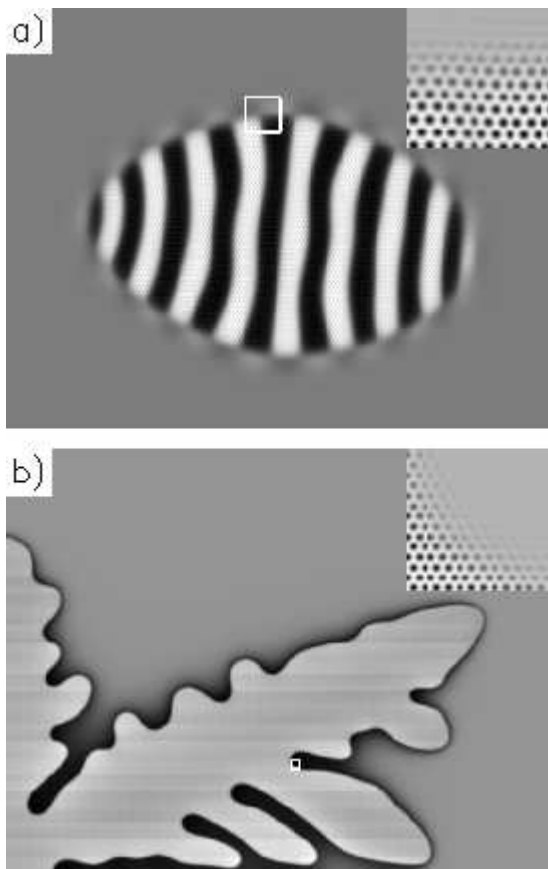


FIG. 7: The grey-scale in the main portion of both figures show the concentration field  $\delta N$ . In the insets, the grey-scale shows the density field,  $n$ , for the small portion of the main figure that is indicated by the white boxes. a) Eutectic crystal grown from a supercooled liquid at  $\Delta B_0 = 0.0248$  and  $\delta N = 0.0$ . The parameters that enter the model are the same as Fig. (5) except  $L = 1.20$  and  $R_1/R_0 = 1/4$ . b) Dendrite crystal grown from a supercooled liquid at  $\Delta B_0 = 0.04$  and  $\delta N = 0.0904$ . The parameters that enter the model are the same as Fig. (3) except  $L = 1.20$  and  $R_1/R_0 = 1/4$ . In Fig. (b) mirror boundary conditions were used.

that the growth of a single crystal from a supercooled melt in two dimensions. In the first simulation a small perturbation in the density field was introduced into a supercooled liquid using the parameters corresponding to the phase diagram in Fig. (5), except  $L = 1.20$  and  $R_1/R_0 = 1/4$ . The reduced temperature  $\Delta B_0 = 0.0248$  and average concentration of  $\delta N = 0.0$ . To reduce computational time the size of the lattice was gradually increased as the seed increased in size. A snapshot of the seed is shown at  $t = 480,000$  in Fig. (7a). A similar simulation was conducted for the growth of a dendrite from a supercooled melt for reduced temperature  $\Delta B_0 = 0.04$  and  $\delta N = 0.0904$ , with other parameters corresponding to those in Fig. (3), except for  $L = 1.20$  and  $R_1/R_0 = 1/4$ . A sample dendritic structure is shown in Fig. (7b) at  $t = 175,000$ .

Simulations such as these can play an important role

in establishing various constitutive relations for use in higher-scale finite element modeling (FEM) of elasto-plastic effects in alloys during deformation. In particular, traditional FEM approaches often employ empirical or experimental constitutive models to describe stress-strain response in elements that are intended to represent one (or more) grains. These constitutive relations are often limited in their usefulness as they do not self-consistently incorporate realistic information about microstructural properties that develop during solidification.

## B. Epitaxial Growth

Another potential application of the PFC model is in the technologically important process of thin film growth. The case of heteroepitaxy, the growth of a crystalline film exhibiting atomic coherency with a crystalline substrate of differing lattice constant, has been examined in previous PFC studies of pure systems [33, 34]. These initial works focused on two of the primary phenomena influencing film quality: (i) morphological instability to buckling or roughening and (ii) dislocation nucleation at the film surface. A third important effect in alloy films, (iii) compositional instability (phase separation in the growing film), requires consideration of multiple atomic species and their interaction. The purpose of this section is to illustrate how the binary PFC model addresses such compositional effects in alloy heteroepitaxy, focusing on the spatial dynamics of phase separation over diffusive time scales.

To date, a number of models of single component film growth incorporating surface roughening, dislocation nucleation, or both have been proposed [25, 55, 56, 57, 58, 59, 60, 61, 62, 63], and models of binary film growth incorporating surface roughening and phase separation have been proposed as well [64, 65, 66, 67]. However, no existing models of binary film growth known to the authors have captured all of the above important phenomena, and it would be reasonable to expect that new insights into the nature of film growth could be gained through the simultaneous investigation of all of these growth characteristics. A unified treatment of this sort is required for the following reasons. There is clearly a strong link between surface roughening and dislocation nucleation, originating from the fact that dislocations nucleate at surface cusps when the film becomes sufficiently rough. It is also known that phase separation in the film is significantly influenced by local stresses, which are inherently coupled to surface morphology and dislocation nucleation. The dynamics of the growth process must then be influenced by the cooperative evolution of all three of these phenomena. In the next subsection numerical simulations will be presented to show that the binary PFC model produces all of the growth characteristics described above, and that each is influenced by misfit strain and atomic size and mobility differences between species.

### 1. Numerical simulations

The physical problem recreated in these simulations is that of growth of a symmetric (50/50 mixture,  $\delta N_0 = 0$ ) binary alloy film from a liquid phase or from a saturated vapor phase above the bulk coherent spinodal temperature ( $\Delta T_c$ ). Growth at temperatures above the miscibility gap is typical of experimental conditions and should ensure that phase separation is driven by local stresses and is not due to spinodal decomposition. Initial conditions consisted of a binary, unstrained crystalline substrate, eight atoms in thickness, placed below a symmetric supercooled liquid of components  $A$  and  $B$ . In all the simulations presented, parameters are the same as in Fig. (2) except for  $L = 1.882$  and  $\Delta B = 0.00886$  unless specified in the figure caption. In what follows the misfit strain,  $\epsilon$ , is defined as  $(a_{film} - a_{sub})/a_{sub}$ , where  $a_{film} \approx a_A(1 + \eta\delta N_0)$  if in the constant concentration approximation. For a symmetric mixture of  $A$  and  $B$  atoms (i.e.,  $\delta N_0 = 0$ )  $a_{film} = (a_A + a_B)/2$ .

Periodic boundary conditions were used in the lateral directions, while a mirror boundary condition was applied at the bottom of the substrate. A constant flux boundary condition was maintained along the top boundary,  $120\Delta x$  above the film surface, to simulate a finite deposition rate. Misfit strain was applied to the system by setting  $R = 1$  in the substrate and  $R = 1 + \epsilon + \eta\delta N$  in the film. This approach yields a film and substrate that are essentially identical in nature except for this shift in lattice parameter in the film. Complexities resulting from differing material properties between the film and substrate are therefore eliminated, isolating the effects of misfit strain, solute strain, and mobility differences on the film growth morphology. The substrate was permitted to strain elastically, but was prevented from decomposing compositionally except near the film/substrate interface.

A sample simulation is shown in Fig. (8) for a misfit strain of  $\epsilon = 0.04$ , a solute expansion coefficient of  $\eta = -1/4$  and mobilities  $M_A = M_B = 1$ . As seen in this figure the well-documented buckling or Asaro-Tiller-Grinfeld [56, 57] instability is naturally reproduced by the PFC model. This instability is ultimately suppressed as a cusp-like surface morphology is approached, with increasingly greater stress developing in surface valleys. The buckling behavior ceases only when the local stress in a given valley imparts on the film a greater energy than that possessed by an equivalent film with a dislocation. At this stage a dislocation is nucleated in the surface valley and the film surface begins to approach a planar morphology.

The nature of phase separation within the bulk film and at the film surface was found to vary with model parameters, but a number of generalizations applicable to all systems studied have been identified. For the case of equal mobilities ( $M_A = M_B$ ) we find that in the presence of misfit and solute strain, the component with greater misfit relative to the substrate preferentially seg-

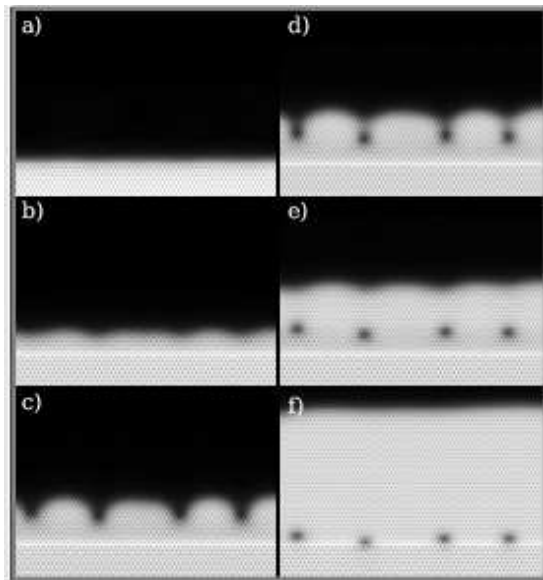


FIG. 8: Plots of the smoothed local free energy showing the progression of the buckling instability, dislocation nucleation and climb towards the film/substrate interface. From a) to f) times shown are  $t=150, 600, 1050, 1200, 1500$  and  $2550$ . In this figure  $\epsilon = 0.04$ ,  $\eta = -1/4$  and  $M_A = M_B = 1$ .

regates below surface peaks (see regions marked 1 and 2 in Fig. (9) and Fig. (10)). Larger (smaller) atoms will be driven toward regions of tensile (compressive) stress which corresponds to peaks (valleys) in a compressively strained film and to valleys (peaks) in a film under tensile strain. This coupling creates a lateral phase separation on the length scale of the surface instability and has been predicted and verified for binary films [64, 65, 66, 67, 68, 69, 70, 71, 72] and analogous behavior has been predicted and verified in quantum dot structures [73, 74, 75].

Secondly, again for the case of equal mobilities, the component with greater misfit relative to the substrate is driven toward the film surface (see Fig. (10)). This behavior can also be explained in terms of stress relaxation and is somewhat analogous to impurity rejection in directional solidification. The greater misfit component can be viewed as an impurity that the growing film wishes to drive out toward the interface. Experimental evidence from SiGe on Si [68] and InGaAs on InP [69, 70] verifies this behavior as an enrichment of the greater misfit component was detected at the film surface in both systems. Other models [64, 65, 66, 67] have not led to this type of vertical phase separation possibly due to neglecting diffusion in the bulk films.

The third generalization that can be made is that, in the case of sufficiently unequal mobilities, the component with greater mobility accumulates at the film surface (see region marked 3 in Fig. (9)). It was found that when the two components have a significant mobility difference (typically greater than a 2:1 ratio) the effect of

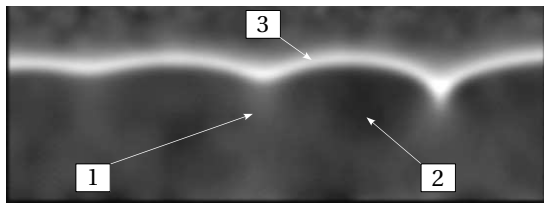


FIG. 9: Plot of the smoothed local concentration field showing lateral phase separation between the surface peaks and valleys. White: Component A (large, fast), Black: Component B (small, slow). In this figure  $\epsilon = -0.02$ ,  $\eta = 0.4$ ,  $M_A = 1$ ,  $M_B = 1/4$ , and  $t = 3500$ . See text for discussion of the numbered arrows.

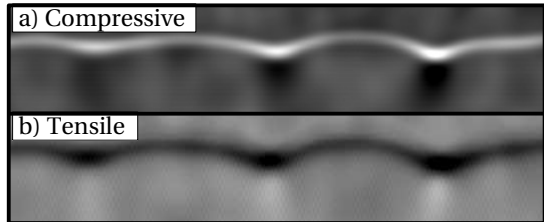


FIG. 10: Plot of the smoothed local concentration field showing the nature of the phase separation under opposite signs of  $\epsilon$ . In figures a) and b)  $\epsilon = 0.04$  and  $-0.025$  respectively and in both figures  $M_A = M_B = 1$  and  $\eta = 0.25$ .

mobility is more important than the combined effects of misfit and solute strains in determining which component accumulates at the surface. Since Ge is believed to be the more mobile component in the SiGe system, we see that the findings of Walther et al [68] for SiGe on Si provide experimental support for this claim. They find a significant enrichment of Ge at the film surface, a result that was likely due to a combination of this mobility driven effect as well as the misfit driven effect described in the second generalization. Experimental evidence also indicates that segregation of substrate constituents into the film may occur during film growth [76, 77]. We have similarly found that a vertical phase separation can be produced near the film/substrate interface and is complimented by a phase separation mirrored in direction near defects (see Fig. (11)). The extent of this phase separation is controlled largely by the bulk mobilities of the two constituents, and to a lesser degree by  $\eta$ . The complimenting phase separation near climbing defects is a transient effect, any traces of which are dulled once the defect reaches the film/substrate interface.

### C. The Role of Dislocations in Spinodal Decomposition

Spinodal decomposition is a non-equilibrium process in which a linearly unstable homogenous phase spontaneously decomposes into two daughter phases. An example of this process in the solid state occurs during

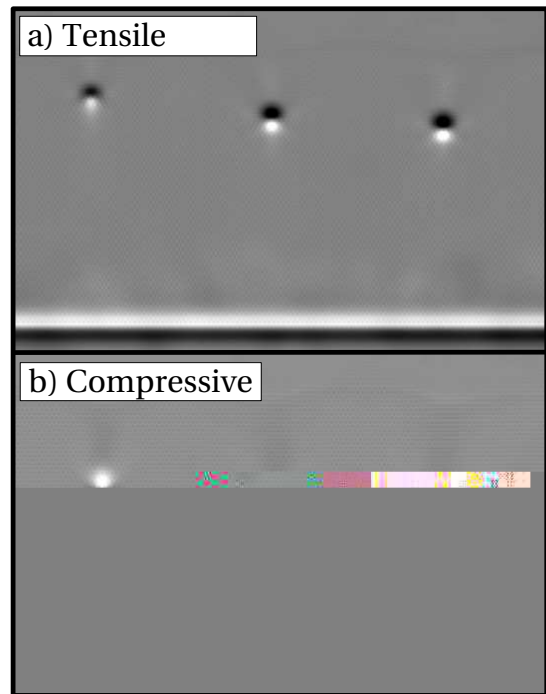


FIG. 11: Plot of the smoothed local concentration field showing the complimentary phase separation at the film/substrate interface and around defects. In this figure the film/liquid interface cannot be distinguished due to the overwhelming contrast created near the defects and at the film/substrate interface. In figures a) and b)  $\epsilon = -0.035$  and  $0.05$  respectively, and in both figures  $M_A = M_B = 1$  and  $\eta = 1/4$ .

a quench below the spinodal in Fig. (3) when  $\delta N = 0$ . During this process domains of alternating concentration grow and coarsen to a tens of nanometers. Spinodal decomposition is of interest as it is a common mechanism for strengthening alloys, due to the large number of interfaces that act to impede dislocation motion.

Solid state strengthening mechanisms, such as spinodal decomposition, rely critically on the interactions that exist between dislocations and phase boundaries. Cahn was first to calculate that the driving force for nucleation of an incoherent second phase precipitate is higher on a dislocation than in the bulk solid [48]. A similar result was obtained by Dolins for a coherent precipitate with isotropic elastic properties in the solid solution [47]. Hu et. al confirmed the results of Cahn and Dolins using a model that included elastic fields from compositional inhomogeneities and structural defects [50].

Recent studies of spinodal decomposition have used phase field models to examine the role of dislocations on alloy hardening [46, 49]. These phase field models couple the effects of static dislocations to the kinetics of phase separation. Léonard and Desai were the first to simulate the effect of static dislocations on phase boundaries, showing that the presence of dislocations strongly favors the phase separation of alloy components [45].

Haataja et al. recently introduced mobile dislocations

into a phase field model that couples two burgers vectors fields to solute diffusion and elastic strain relaxation. It was shown that mobile dislocations altered the early and intermediate time coarsening regime in spinodal decomposition [43, 78]. Specifically, it was found that coherent strain at phase boundaries decrease the initial coarsening rate, since they increase stored elastic energy in the system. As dislocations migrate toward moving interfaces, they relax the excess the strain energy, thus increasing the coarsening rate [78]. The growth regimes predicted by the model in Ref. [78] are in general agreement with several experimental studies of deformation on spinodal age hardening [38, 39, 42, 44].

### 1. Numerical Simulations

The findings of Ref. [78] were compared with numerical simulations from the alloy PFC model. Here, spinodal decomposition was simulated for an alloy corresponding to the phase diagram in Fig. (3). Simulations began with a liquid phase of average dimensionless density difference  $\delta N = 0$ , which first solidified into a polycrystalline solid (alpha) phase, which subsequently phase separated as the reduced temperature ( $\Delta B_o$ ) was lowered below the spinodal. Figure (12) shows the concentration and density fields for four time sequences during the spinodal decomposition process. The dots in the figures denote the locations of dislocation cores. Parameters for this simulation are given in the figure caption. Figure (13) shows a plot of the average domain size versus time corresponding to the data in Figure (12).

The PFC alloy results are in general agreement the results of Ref. [78]. Specifically, PFC simulations show an early and intermediate time regime where the spinodal coarsening rate is reduced from its traditional  $t^{1/3}$  behaviour. In this regime, the strain energy stored in the system is found to be much higher than that at late times when dislocations migrate to the boundaries, relaxing strain energy and leading to an an increased coarsening rate toward the usual  $t^{1/3}$  growth law. To more clearly illustrate the the interaction between a coherent boundaries and dislocations, Fig. (14) shows four time steps in the evolution of a dislocation migrating toward a phase boundary to relax mismatch strains.

It is noteworthy that the alloy PFC introduced in this work does not incorporate “instantaneous” elastic relaxation. A proper treatment of rapid relaxation of strain fields requires the model to be extended in a manner analogous to [41]. However, because of the asymptotically slow kinetics of spinodal decomposition and the small length scales between domain boundaries, it is expected that this will only influence the time scales over which dislocations interact with domain boundaries. As a result, the general trends depicted in Figures. (13) and (12) are expected to be correct.

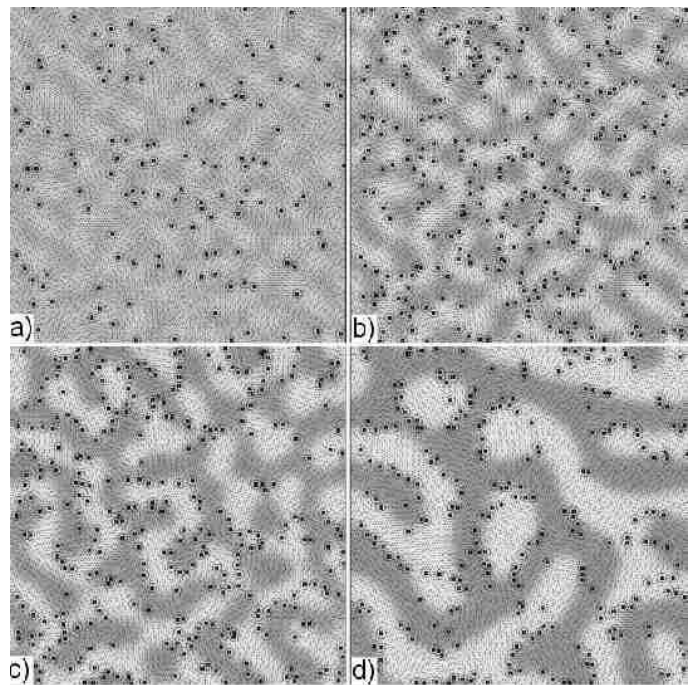


FIG. 12: Four time sequences in the evolution of the concentration field (grey scale), superimposed on the corresponding density field. Dislocations are labeled by a square on the dislocation core surrounded by a circle. The time sequence (a)-(d) corresponds to  $t = 12000, 24000, 60000$  and  $288000$ , respectively (in units of  $\Delta t = 0.004$ ). The system size is:  $1024\Delta x \times 1024\Delta x$ , where  $\Delta x = \pi/4$ . The density difference  $\delta N = 0$ , while  $L = 2.65$ ,  $R_1/R_0 = 0.25$  and all other parameters are the same as Fig. (3).

## VI. DISCUSSION AND CONCLUSIONS

In this paper a connection between the density functional theory of freezing and phase field modeling was examined. More specifically it was shown that the phase field crystal model introduced in earlier publications [33, 34, 35] and the regular solution commonly used in material science can be obtained from DFT in certain limits. These calculations relied on parameterizing the direct two-point correlation function that enters DFT by three quantities related to the elastic energy stored in the liquid and crystalline phases, as well as the lattice constant.

In addition, a simplified binary alloy model was developed that self-consistently incorporates many physical features inaccessible in other phase field approaches. The simplified alloy PFC model was shown to be able to simultaneously model solidification, phase segregation, grain growth, elastic and plastic deformations in anisotropic systems with multiple crystal orientations on diffusive time scales.

It is expected that the alloy PFC formalism and its extensions can play an important role in linking material properties to microstructure development in a manner

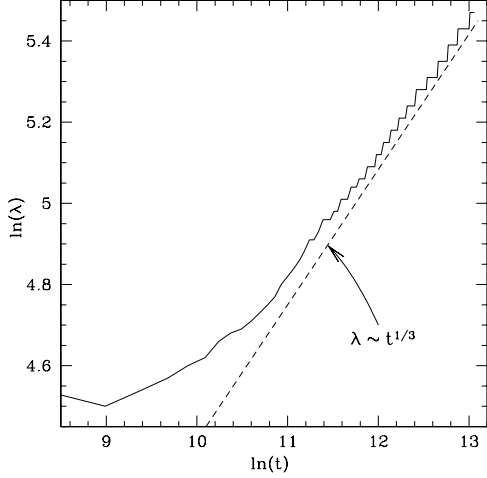


FIG. 13: Inverse of the mean wave vector of the (circularly averaged) 2D structure factor of the concentration field Vs. time corresponding to the simulation in Figure 12.

that *fundamentally* links the meso-scale to the atomic scale. As such this formalism, particularly when combined with novel adaptive mesh techniques in phase-amplitude or reciprocal space, can lead the way to a truly multi-scale methodology for predictive modeling of materials performance.

## VII. ACKNOWLEDGMENTS

K. R. E. acknowledges support from the National Science Foundation under Grant No. DMR-0413062. N. P. and M. G. would like to thank the National Science and Engineering Research Council of Canada for financial support. M. G. also acknowledges support from le Fonds Quebecois de la recherche sur la nature et les technologies. J. B. acknowledges support from the Richard H. Tomlinson Foundation.

## APPENDIX A: NUMERICAL DISCRETIZATION SCHEMES

The governing Equations were numerically solved using two different methods, described below. In what follows the subscripts  $n$ ,  $i$  and  $j$  are integers corresponding to the number of time steps and distance along the  $x$  and  $y$  directions, respectively, of a discrete numerical lattice. Time and space units are recovered by the simple rela-

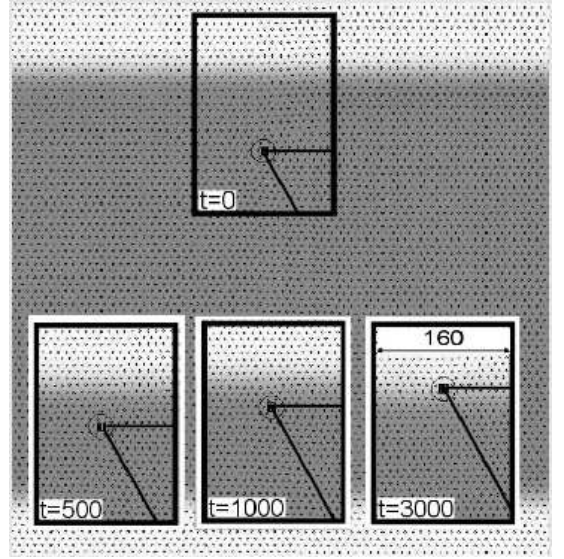


FIG. 14: A dislocation migrates toward a coherent phase boundary thus relaxing mismatch strain. An  $800 \times 800$  (units of  $\Delta x$ ) portion of the actual simulations domain is shown. The data shows four time frames in the motion of the dislocation. Parameters of the simulation are the same as in Figure 12.

tions,  $t = n\Delta t$ ,  $x = i\Delta x$  and  $y = j\Delta x$ .

An Euler discretization scheme was used for the time derivative and the ‘spherical laplacian’ approximation was used to calculate all Laplacians. For this method the discrete dynamics become

$$\psi_{n+1,i,j} = \psi_{n,i,j} + \nabla^2 \mu_{n,i,j}, \quad (\text{A1})$$

where  $\mu_{n,i,j}$  is the chemical potential given by

$$\mu_{n,i,j} = (r + (1 + \nabla^2)^2) \psi_{n,i,j} - \psi_{n,i,j}^3. \quad (\text{A2})$$

All Laplacians were evaluated as follows,

$$\begin{aligned} \nabla^2 f_{n,i,j} = & \left( (f_{n,i+1,j} + f_{n,i-1,j} + f_{n,i,j+1} \right. \\ & + f_{n,i,j-1})/2 + (f_{n,i+1,j+1} + f_{n,i-1,j+1} \\ & + f_{n,i-1,j+1} + f_{n,i-1,j+1})/4 - 3f_{n,i,j} \Big) / (\Delta x)^2 \end{aligned} \quad (\text{A3})$$

## APPENDIX B: FREE ENERGY FUNCTIONAL FOR A PURE MATERIAL

This appendix outlines the derivation of the free energy functional  $\mathcal{F}[\rho]$  presented in Section II A for a non-homogeneous liquid. The derivation follows the standard techniques of classical density functional theory as outlined in [54] (similar approaches are also employed in Ref. [52, 53]).

The derivation begins with the definition of the grand partition function for  $N$  particles at temperature  $T$ ,

$$\Xi = Tr \{ e^{(H_N - \mu N)/k_B T} \} \quad (\text{B1})$$



where

$$Tr \equiv \frac{1}{h^{3N} N!} \sum_{N=0}^{\infty} \int d\vec{r}_1 d\vec{r}_2 \dots d\vec{r}^N \int d\vec{p}_1 d\vec{p}_2 \dots d\vec{p}^N \quad (\text{B2})$$

is the classical trace operator, with  $\vec{r}_i$  and  $\vec{p}_i$  being the position momentum of the  $i^{\text{th}}$  atom, respectively,  $\mu$  is the chemical potential and  $h$  denotes Plank's constant. The N-body hamiltonian is denoted by  $H_N = K + U + V$ , where

$$\begin{aligned} K &= \sum_{i=1}^N \frac{p_i^2}{m_i} \\ U &\equiv U(\vec{r}_1, \dots, \vec{r}_N) \\ V &= \sum_{i=1}^N V_{\text{ext}}(\vec{r}_i) \end{aligned} \quad (\text{B3})$$

Here  $U$  denotes the interaction potential between particles in the the system (including many body interactions),  $K$  is the total kinetic energy, with  $m_i$  the mass of particles  $i$  and  $V_{\text{ext}}$  represents the interaction of atom  $i$  with an external field. The probability density for any particular phase space configuration is given by

$$f_{\text{eq}} = \Xi^{-1} e^{(H_N - \mu N)/k_B T} \quad (\text{B4})$$

The number density operator an N-body system is defined by by

$$\hat{\rho}(\vec{r}) = \sum_{i=1}^N \delta(\vec{r} - \vec{r}_i) \quad (\text{B5})$$

The equilibrium number density is obtained by averaging the density operator with the equilibrium probability density,

$$\rho(\vec{r}) = \langle \hat{\rho} \rangle = Tr\{ \hat{\rho} f_{\text{eq}} \} \quad (\text{B6})$$

The PFC formalism will ultimately yield governing equations for the evolution of the number density in Eq. (B6) on diffusive time scales. It is noteworthy that the equilibrium probability density,  $f_{\text{eq}}$ , is a functional of  $\rho(\vec{r})$  [54], an important property used in the derivation below. This is because for a given  $U$ ,  $V_{\text{ext}}$  is uniquely determined by  $\rho(\vec{r})$ . Moreover, since  $V_{\text{ext}}$  determines  $f_{\text{eq}}$ , it follows that the equilibrium density  $f_{\text{eq}}$  is a functional of  $\rho(\vec{r})$ . The details of this argument are derived rigorously in in Ref. [54] and will not be reproduced here.

The arguments of the previous paragraph also imply that for a given  $U$ , the Helmholtz free energy, defined by

$$\mathcal{F}[\rho] = Tr\{ f_{\text{eq}}(K + U + k_B T \ln f_{\text{eq}}) \} \quad (\text{B7})$$

is also a functional of  $\rho(\vec{r})$  [54], as is also the grand potential functional, defined by

$$\Omega[\rho] = \int d\vec{r} \rho(\vec{r}) V_{\text{ext}}(\vec{r}) + \mathcal{F}[\rho] - \mu \int d\vec{r} \rho(\vec{r}) \quad (\text{B8})$$

It should be noted that the grand potential can be cast into a more familiar form by substituting Eq. (B6) into  $\Omega[\rho]$  and exchanging the order of integration over  $\vec{r}$  and  $Tr$  operation. Specifically, using the straightforward results  $\int d\vec{r} \rho(\vec{r}) V_{\text{ext}}(\vec{r}) = -Tr\{ f_{\text{eq}} V \}$  and  $-\mu \int d\vec{r} \rho(\vec{r}) = -Tr\{ f_{\text{eq}} \mu N \}$ , leads to the well known result from statistical mechanics,

$$\Omega[\rho] \equiv -k_B T \ln \Xi \quad (\text{B9})$$

The grand potential is important in that it can be used to relate the chemical potential to the equilibrium density  $\rho(\vec{r})$  according to  $\delta\Omega[\rho]/\delta\rho(\vec{r}) = 0$  which gives [54]

$$\mu = V_{\text{ext}}(\vec{r}) + \frac{\delta\mathcal{F}[\rho]}{\delta\rho(\vec{r})} \quad (\text{B10})$$

Equation (B10) is fundamental to the theory of non-uniform fluids in as it can, in principle, be used to calculate the equilibrium density [53, 54].

The properties of the free energy functional  $\mathcal{F}[\rho]$  can be better elucidated by writing it as the sum of two terms

$$\mathcal{F}[\rho] = \mathcal{F}_0[\rho] - \Phi[\rho] \quad (\text{B11})$$

where  $\mathcal{F}_0$  represents the ideal case of non-interacting particles, while  $\Phi[\rho]$  represents the total potential energy of interactions between the particles. Note that for a given  $U$ ,  $\Phi$  is, once again, a functional of  $\rho(\vec{r})$ . Moreover, for  $U = 0$  in Eq. (B7)  $\mathcal{F}_0[\rho]$  becomes

$$\mathcal{F}_0[\rho] = k_B T \int d\vec{r} \rho(\vec{r}) (\ln(\lambda \rho(\vec{r})) - 1) \quad (\text{B12})$$

where  $\lambda = \sqrt{(h^2/2m\pi k_B T)}$  [54].

To further discuss the properties of  $\mathcal{F}[\rho]$  for periodic phases, it will be useful to expand the free energy in Eq. (B11) about the density,  $\rho = \rho_l$ , which corresponds to the liquid side of the solid-liquid coexistence phase diagram (at a given temperature). The change in free energy,  $\mathcal{F}_c \equiv \mathcal{F}[\rho] - \mathcal{F}[\rho_l]$ , then becomes

$$\mathcal{F}_c = (\mathcal{F}_0[\rho] - \mathcal{F}_0[\rho_l]) - (\Phi[\rho] - \Phi[\rho_l]) \quad (\text{B13})$$

The first term on the right hand side of Eq. (B13) can be simplified by substituting  $\rho = \rho_l + \delta\rho$  in the non-logarithmic expressions of  $\mathcal{F}_0[\rho]$ , giving

$$(\mathcal{F}_0[\rho] - \mathcal{F}_0[\rho_l]) = k_B T \int d\vec{r} (\rho \ln(\rho/\rho_l) - \delta\rho) \quad (\text{B14})$$

In arriving at Eq. (B14), use was made of the property  $\int d\vec{r} \delta\rho = 0$  in the periodic state. The interaction term,  $(\Phi[\rho] - \Phi[\rho_l])$ , can also be expanded functionally in  $\delta\rho(\vec{r})$  about  $\rho_l$  by defining

$$\begin{aligned} C_1(\vec{r}) &\equiv \frac{\delta\Phi[\rho(\vec{r})]}{\delta\rho(\vec{r})} \\ C_2(\vec{r}_1, \vec{r}_2) &\equiv \frac{\delta^2\Phi}{\delta\rho(\vec{r}_1)\delta\rho(\vec{r}_2)} \\ C_3(\vec{r}_1, \vec{r}_2, \vec{r}_3) &\equiv \frac{\delta^3\Phi}{\delta\rho(\vec{r}_3)\delta\rho(\vec{r}_1)\delta\rho(\vec{r}_2)} \\ &\dots \end{aligned} \quad (\text{B15})$$

Using Eq. (B14) and (B15) in Eq. (B13) finally gives

$$\begin{aligned} \frac{\mathcal{F}_c}{k_B T} &= \int d\vec{x} \left[ \rho(\vec{r}) \ln \left( \frac{\rho(\vec{r})}{\rho_l} \right) - \delta\rho(\vec{r}) \right] \\ &- \frac{1}{2} \int d\vec{r}_1 d\vec{r}_2 \delta\rho(\vec{r}_1) C_2(\vec{r}_1, \vec{r}_2) \delta\rho(\vec{r}_2) + \\ &- \frac{1}{6} \int d\vec{r}_1 d\vec{r}_2 d\vec{r}_3 \delta\rho(\vec{r}_1) C_3(\vec{r}_1, \vec{r}_2, \vec{r}_3) \delta\rho(\vec{r}_2) \delta\rho(\vec{r}_3) \\ &+ \dots \end{aligned} \quad (\text{B16})$$

The function  $C_2$  is the two point direct correlation function of an isotropic fluid and it is usually denoted  $C_{ij} \equiv C_2(r_{12})$ , where  $r_{12} \equiv |\vec{r}_1 - \vec{r}_2|$ . The function  $C_3$  is the three point correlation function, etc.

### APPENDIX C: SIMPLE BINARY ALLOY MODEL

This appendix goes through the expansion required to arrive at the simplified alloy model presented in section III B. The starting point is the definition of the following three fields,

$$\begin{aligned} n &= (\rho - \bar{\rho})/\bar{\rho} \\ n_A &= (\rho_A - \bar{\rho}_A)/\bar{\rho} \\ n_B &= (\rho_B - \bar{\rho}_B)/\bar{\rho} \end{aligned} \quad (\text{C1})$$

where overbars denote averages. The field  $n$  can equivalently be written as

$$n = n_A + n_B = (\rho_A + \rho_B)/\bar{\rho} - (\bar{\rho}_A + \bar{\rho}_B)/\bar{\rho} \quad (\text{C2})$$

Furthermore, the definitions of  $c = \rho_A/\rho$  and  $\delta c = 1/2 - c$  (see Section III B) can be used to re-write

$$\delta c = \frac{\rho_B - \rho_A}{2\rho} = \frac{\bar{\rho}(n_B - n_A) + \bar{\rho}_B - \bar{\rho}_A}{2\rho}, \quad (\text{C3})$$

which can further be used to define a new field

$$\delta N \equiv 2\rho\delta c/\bar{\rho} = (n_B - n_A) + \frac{\bar{\rho}_B - \bar{\rho}_A}{\bar{\rho}}. \quad (\text{C4})$$

Next, the fields  $\rho$ ,  $\delta\rho = \rho - \rho_l$ ,  $c$  and  $\delta c$  in Eq. (22) are expressed in terms of  $n$  and  $\delta N$ . Following that the free energy is expanded with respect to  $n$  and  $\delta N$  up to order four (noting that terms of order  $n$  or  $\delta N$  can be dropped since they integrate to zero in the free energy functional as they are all defined around their average

values). Carrying out these expansions gives,

$$\begin{aligned} \frac{\mathcal{F}}{\bar{\rho}k_B T} &= \int d\vec{r} \left[ f_o + \frac{n}{2} \left( 1 - \bar{\rho} \frac{C_{AA} + C_{BB} + 2C_{AB}}{4} \right) n \right. \\ &- \frac{n^3}{6} + \frac{n^4}{12} + \frac{\beta}{2\bar{\rho}} (1 - n + n^2 - n^3) \delta N \\ &+ \frac{C_{AA} - C_{BB}}{4\bar{\rho}} \left( (\bar{\rho} - \rho_\ell)^2 + (\bar{\rho}^2 - \rho_\ell^2) n \right. \\ &+ \rho_\ell^2 (n^2 - n^3) \left. \right) \delta N \\ &+ \frac{\delta N}{2} \left( 1 - \frac{C_{AA} + C_{BB} - 2C_{AB}}{4} \right) \delta N \\ &\left. - (n - n^2) \frac{\delta N^2}{2} + \frac{\delta N^4}{12} \right] \end{aligned} \quad (\text{C5})$$

where

$$\begin{aligned} f_o &= \ln \left( \frac{\bar{\rho}}{2\rho_\ell} \right) - (1 - \rho_\ell/\bar{\rho}) - \bar{\rho} C_{AB}^0/4 \\ &- \frac{1}{8} (\bar{\rho} + 2\rho_\ell^2/\bar{\rho} - 4\rho_\ell) (C_{AA}^0 + C_{BB}^0) \end{aligned} \quad (\text{C6})$$

Simplifying further, paying particular attention to the  $n^2$  terms and substituting the explicit forms for  $C_{i,j}^n$  gives,

$$\begin{aligned} \frac{\mathcal{F}}{\bar{\rho}k_B T} &= \int d\vec{r} \left[ f_o + B^\ell \frac{n^2}{2} - \frac{n^3}{6} + \frac{n^4}{12} + nF\nabla^2 n + nG\nabla^4 n \right. \\ &+ \frac{\beta}{2\bar{\rho}} (1 - n - n^3) \delta N \\ &+ \frac{C_{AA} - C_{BB}}{4\bar{\rho}} \left( (\bar{\rho} - \rho_\ell)^2 + (\bar{\rho}^2 - \rho_\ell^2) n \right. \\ &\left. - \rho_\ell^2 n^3 \right) \delta N \\ &+ \frac{\delta N}{2} \left( 1 - \frac{C_{AA} + C_{BB} - 2C_{AB}}{4} \right) \delta N \\ &\left. - \frac{\delta N^2}{2} n + \frac{\delta N^4}{12} \right] \end{aligned} \quad (\text{C7})$$

where

$$\begin{aligned} B^\ell &= 1 - \bar{\rho} (C_{AA}^o + C_{BB}^o + 2C_{AB}^o)/4 \\ &+ \left( \frac{\beta}{\bar{\rho}} + \frac{\rho_\ell^2}{2\bar{\rho}} (C_{AA}^o - C_{BB}^o) \right) \delta N + \delta N^2 \\ F &= -\bar{\rho} (C_{AA}^2 + C_{BB}^2 + 2C_{AB}^2)/4 \\ &+ \frac{\rho_\ell^2}{2\bar{\rho}} (C_{AA}^2 - C_{BB}^2) \delta N \\ G &= -\bar{\rho} (C_{AA}^4 + C_{BB}^4 + 2C_{AB}^4)/4 \\ &+ \frac{\rho_\ell^2}{2\bar{\rho}} (C_{AA}^4 - C_{BB}^4) \delta N \end{aligned} \quad (\text{C8})$$

In what follows it is assumed that  $\delta N$  varies on length scales much larger than  $n$ . This is a reasonable on long time (diffusion) times scales, where solute and host atoms

intermix on length scales many times larger than the atomic radius. This assumption allows terms of order  $n$  to be eliminated from the free energy, i.e.,

$$\begin{aligned} \frac{\mathcal{F}}{\bar{\rho}k_B T} = & \int d\vec{r} \left[ f_o + B^\ell \frac{n^2}{2} - \frac{n^3}{6} + \frac{n^4}{12} + nF\nabla^2 n + nG\nabla^4 n \right. \\ & + \frac{\delta N}{2} \left( 1 - \frac{C_{AA} + C_{BB} - 2C_{AB}}{4} \right) \delta N + \frac{\delta N^4}{12} \\ & + \frac{\beta}{2\bar{\rho}} (1 - n^3) \delta N \\ & \left. + \frac{C_{AA} - C_{BB}}{4\bar{\rho}} \left( (\bar{\rho} - \rho_\ell)^2 - \rho_\ell^2 n^3 \right) \delta N \right] \quad (C9) \end{aligned}$$

The previous equation can finally be cast into a form similar to that presented in Section III C of the text,

$$\begin{aligned} \frac{\mathcal{F}}{\bar{\rho}k_B T} = & \int d\vec{r} \left[ f_o + \frac{n}{2} [B^\ell + B^s (2R^2 \nabla^2 + R^4 \nabla^4)] n \right. \\ & - \frac{n^3}{6} + \frac{n^4}{12} + \frac{w}{2} \delta N^2 + \frac{\delta N^4}{12} + \frac{L^2}{2} |\nabla \delta N|^2 \\ & \left. + \gamma \delta N + \frac{H^4}{2} \delta N \nabla^4 \delta N \right] \quad (C10) \end{aligned}$$

where

$$\begin{aligned} B^s &= F^2 / (2G) \\ R &= \sqrt{2G/F} \\ w &= (1 - (C_{AA}^0 + C_{BB}^0 - 2C_{AB}^0) / 2) \\ L^2 &= (C_{AA}^2 + C_{BB}^2 - 2C_{AB}^2) / 2 \\ H^2 &= -(C_{AA}^4 + C_{BB}^4 - 2C_{AB}^4) / 2 \\ \gamma &= \frac{\beta}{2\bar{\rho}} (1 - n^3) \\ &+ \frac{C_{AA} - C_{BB}}{4\bar{\rho}} \left( (\bar{\rho} - \rho_\ell)^2 - \rho_\ell^2 n^3 \right) \quad (C11) \end{aligned}$$

The dependence of the coefficients in  $B^l$ ,  $B^\ell$  and  $R$  on the density difference can be explicitly obtained by expanding them in  $\delta N$  as well. This gives,

$$\begin{aligned} B^\ell &= B_0^\ell + B_1^\ell \delta N + B_2^\ell \delta N^2 \\ B^s &= B_0^s + B_1^s \delta N + B_2^s \delta N^2 + \dots \\ R &= R_0 + R_1 \delta N + R_2 \delta N^2 + \dots \quad (C12) \end{aligned}$$

where

$$\begin{aligned} B_0^\ell &= 1 - \bar{\rho} \hat{C}_0 \\ B_1^\ell &= \frac{\beta}{\bar{\rho}} + \frac{\rho_\ell^2}{2\bar{\rho}} \delta \hat{C}_0 \\ B_2^\ell &= 1 \quad (C13) \end{aligned}$$

and

$$\begin{aligned} \hat{C}_n &\equiv (C_{AA}^{(n)} + C_{BB}^{(n)} + 2C_{AB}^{(n)}) / 4 \\ \delta \hat{C}_n &\equiv C_{AA}^{(n)} - C_{BB}^{(n)}, \quad (C14) \end{aligned}$$

while

$$\begin{aligned} B_0^s &= -\bar{\rho} \frac{(\hat{C}_2)^2}{\hat{C}_4} \\ B_1^s &= -\frac{\hat{C}_2 \rho_\ell^2}{4\bar{\rho} \hat{C}_4^2} (\hat{C}_2 \delta \hat{C}_4 - 2\hat{C}_4 \delta \hat{C}_2) \\ B_2^s &= -\frac{\rho_\ell^2}{8\bar{\rho}^3 \hat{C}_4^3} (\hat{C}_2 \delta \hat{C}_4 - \hat{C}_4 \delta \hat{C}_2)^2 \quad (C15) \end{aligned}$$

and

$$\begin{aligned} R_0 &= \sqrt{\frac{2\hat{C}_4}{\hat{C}_2}} \\ R_1/R_0 &= -\frac{\rho_\ell^2}{4\bar{\rho}^2 \hat{C}_4 \hat{C}_2} (\hat{C}_2 \delta \hat{C}_4 - \hat{C}_4 \delta \hat{C}_2) \\ R_2/R_0 &= -\frac{\rho_\ell^4}{32\bar{\rho}^4 \hat{C}_4^2 \hat{C}_2^2} (\hat{C}_2 \delta \hat{C}_4 - \hat{C}_4 \delta \hat{C}_2) \times \\ & \quad (\hat{C}_2 \delta \hat{C}_4 + 3\hat{C}_4 \delta \hat{C}_2) \quad (C16) \end{aligned}$$

- 
- [1] J. W. Cahn and J. E. Hilliard, *J. Chem. Phys.* **28**, 258 (1958); H. E. Cook, *Acta Metall.* **18**, 297 (1970).  
[2] S. M. Allen and J. W. Cahn, *Acta Metall.* **23** (1975); *ibid* **24**, 425 (1976); *ibid* **27**, 1085 (1979).  
[3] L. Leibler, *Macromolecules* **13**, 1602 (1980); Y. Oono and Y. Shiwa, *Mod. Phys. Lett. B* **1**, 49 (1987).  
[4] J. B. Collins and H. Levine, *Phys. Rev. B* **31**, 6119 (1985).  
[5] J. S. Langer in *Directions in Condensed Matter* (World

- Scientific, Singapore 1986), p. 164.  
[6] B. Grossmann, K. R. Elder, M. Grant and J. M. Kosterlitz, *Phys. Rev. Lett.*, **71**, 3323 (1993).  
[7] K. R. Elder, F. Drolet, J. M. Kosterlitz and M. Grant, *Phys. Rev. Lett.*, **72**, 677 (1994); F. Drolet, K. R. Elder, M. Grant and J. M. Kosterlitz *Phys. Rev. E*, **61**, 6705 (2000).  
[8] J. A. Warren and W. J. Boettinger, *Acta Metall. Mater.* **A**, **43**, 689 (1995).

- [9] G. Caginalp and X. Chen in *On the Evolution of Boundaries*, edited by M.E. Gurtin and G. B. McFadden, IMA Volumes in Mathematics and its Applications, **43** (Springer-Verlag, New York, 1992), p. 1.
- [10] R. Kobayashi, *Physica D*, **63**, 410 (1993).
- [11] S-L. Wang, R. F. Sekerka, A. A. Wheeler, B. T. Murray, S. R. Coriell, R. J. Braun and G. B. McFadden, *Physica D*, **69**, 189 (1993).
- [12] A. Karma and W.-J. Rappel *Phys. Rev. E* **53**, R3017 (1996).
- [13] A. Karma *Phys. Rev. Lett.* **87**, 115701 (2001).
- [14] K. R. Elder, M. Grant, N. Provatas and J. M. Kosterlitz, *Phys. Rev. E* **64**, 21604 (2001).
- [15] N. Provatas, M. Greenwood, B. Athreya, N. Goldenfeld and J. Dantzig", *International Journal of Modern Physics B* **19**, 4525 (2005)
- [16] N. Provatas, N. Goldenfeld and J. Dantzig *Phys. Rev. Lett.* **80**, 3308 (1998).
- [17] N. Provatas, J. Dantzig and N. Goldenfeld *J. Comp. Phys.* **148**, 265 (1999).
- [18] N. Provatas, N. Goldenfeld, J. Dantzig, J. C. LaCombe, A. Lupulescu, M. B. Koss, M. E. Glicksman and R. Almgren, *Phys. Rev. Lett.* **82**, 4496 (1999).
- [19] N. Provatas, Q. Wang, M. Haataja, and M. Grant, *Phys. Rev. Lett.*, **91**, 155502 (2003).
- [20] C.W. Lan, Y.C. Chang, and C.J. Shih, *Acta Mater.* **51**, 1857 (2003).
- [21] M. Greenwood, M. Haataja, and N. Provatas, *Phys. Rev. Lett.*, **93**, 246101 (2004).
- [22] C.W. Lan, and C.J. Shih, *J. Cryst. Growth*, **264** 472 (2004).
- [23] Y. U. Wang, Y. M. Jin, A. M. Cuitino, and A. G. Khachaturyan, *Appl. Phys. Lett.* **78**, 2324 (2001); *Philos. Mag. Lett.* **81**, 385 (2001); *Acta Mater.* **49**, 1847 (2001).
- [24] Y. M. Jin and A. G. Khachaturyan, *Philos. Mag. Lett.* **81**, 607 (2001).
- [25] M. Haataja, J. Müller, A. D. Rutenberg, and M. Grant, *Phys. Rev. B* **65**, 165414 (2002).
- [26] Y. Wang and A. G. Khachaturyan, *Acta. Mater.* **43**, 1837 (1995); *Acta. Mater.* **45**, 759 (1997).
- [27] L. Q. Chen and A. G. Khachaturyan, *Script. Metall. et Mater.* **25**, 61 (1991)
- [28] L.-Q. Chen and W. Yang, *Phys. Rev. B* **50** 15752 (1994)
- [29] B. Morin, K. R. Elder, M. Sutton and M. Grant, *Phys. Rev. Lett.*, **75**, 2156 (1995).
- [30] J. A. Warren, W. C. Carter, and R. Kobayashi, *Physica (Amsterdam)* **261A**, 159 (1998); *J. A. Warren, R. Kobayashi and W. C. Carter, J. Cryst. Growth* **211**, 18 (2000); *R. Kobayashi, J. A. Warren and W. C. Carter, Physica D.* **140D** 141 (2000).
- [31] J. A. Warren, R. Kobayashi, A. E. Lobkovsky, and W. C. Carter, *Acta Materialia*, **51**, 6035 (2003).
- [32] L. Granasy, T. Pusztai, and J. A. Warren, *J. Phys.: Condens. Matter*, **16** R1205 (2004); *L. Granasy, T. Pusztai, T. Borzsonyi, J. A. Warren, B. Kvamme, and P. F. James, Phys. Chem. Glasses* **45**, 107 (2004).
- [33] K. R. Elder, M. Katakowski, M. Haataja and M. Grant, *Phys. Rev. Lett.*, **88** 245701 (2002).
- [34] K. R. Elder and M. Grant, *Phys. Rev. E*, **70** 051605 (2004).
- [35] J. Berry, M. Grant, and K. R. Elder, *Phys. Rev. E* **73**, 031609 (2006).
- [36] Y. M. Jin and A. G. Khachaturyan, private communication (2006).
- [37] N. Goldenfeld, B. P. Athreya, and J. A. Dantzig, *Phys. Rev. E*, **72**, 020601(R) (2005)
- [38] S. Spooner and B.G. Lefevre, *Metall. Trans. A* **11A**, 1085 (1975).
- [39] F.T. Helmi and L. Zsoldos, *Scr. Metall.* **11**, 899 (1977).
- [40] N. Goldenfeld, B. P. Athreya, and J. A. Dantzig, to appear *J. Stat. Phys.*.
- [41] P. Stefanovic and M. Haataja and N.Provatas, *Phys. Rev. Lett.* **96**, 225504 (2006).
- [42] R. R. Bhat and P. P. Rao, *Z. Metallkd.* **75**, 237 (1994).
- [43] Mikko Haataja and Francois Léonard, *Phys. Rev. B* **69**, 081201(R) (2004).
- [44] J. T. Plewes, *Metall. Trans. A* **6A**, 537 (1975).
- [45] F. Léonard and R.C Desai, *Phys. Rev. B* **58**, 8277 (1998).
- [46] D. Rodney, Y. Le Bouar, and A. Finel, *Acta Metall.* **51**, 17 (2003).
- [47] C.C. Dolins, *Acta Metall.* **18**, 1209 (1970).
- [48] J.W. Cahn, *Acta Metall.* **5**, 169 (1957).
- [49] J.W. Cahn, *Acta Metall.* **11**, 1275 (1963).
- [50] S.Y. Hu and L.Q. Chen, *Acta Metall.* **49**, 463 (2001).
- [51] K-A Wu and A. Karma, private communication (2006).
- [52] T. V. Ramakrishnan and M. Yussouff, *Phys. Rev. B*, **19** 2775 (1979).
- [53] Y. Singh, *Physics Reports* **207**, No 6, 351 (1991).
- [54] R. Evans *Advances in Physics*, **28**, No. 2,143 (1979)
- [55] J. W. Matthews and A. E. Blakeslee, *J. Cryst. Growth* **27**, 118 (1974). *J. W. Matthews, J. Vac. Sci. Technol.* **12** 126 (1975).
- [56] R. J. Asaro and W. A. Tiller, *Metall. Trans.* **3**, 1789 (1972).
- [57] M. Grinfeld, *J. Nonlin. Sci.* **3**, 35 (1993); *Dokl. Akad. Nauk SSSR* **290**, 1358 (1986); [*Sov. Phys. Dokl.* **31**, 831 (1986)].
- [58] R. People and J. C. Bean, *Appl. Phys. Lett.* **47**, 322 (1985).
- [59] J. Müller and M. Grant, *Phys. Rev. Lett.* **82**, 1736 (1999).
- [60] W. H. Yang and D. J. Srolovitz, *Phys. Rev. Lett* **71**, 1593 (1993).
- [61] K. Kassner, C. Misbah, J. Müller, J. Kappey, and P. Kohlert, *Phys. Rev. E* **63**, 036117 (2001).
- [62] J. Tersoff and F. K. LeGoues, *Phys. Rev. Lett* **72**, 3570 (1994).
- [63] H. Gao and W. D. Nix, *Annu. Rev. Mater. Sci.* **29**, 173 (1999).
- [64] B. J. Spencer, P. W. Voorhees, and J. Tersoff, *Phys. Rev. Lett.* **84**, 2449, 2000; *Phys. Rev. B* **64**, 235318, 2001.
- [65] J. E. Guyer and P. W. Voorhees, *Phys. Rev. B* **54**, 11710 (1996); *Phys. Rev. Lett.* **74**, 4031 (1995); *J. Cryst. Growth* **187**, 150 (1998).
- [66] Z. F. Huang and R. C. Desai, *Phys. Rev. B* **65**, 195421, 2002; *Phys. Rev. B* **65**, 205419, 2002.
- [67] F. Leonard and R. C. Desai, *Phys. Rev. B* **56**, 4955, 1997. *Phys. Rev. B* **57**, 4805, 1998.
- [68] T. Walther, C. J. Humphries, and A. G. Cullis, *Appl. Phys. Lett.* **71**, 809, 1997.
- [69] T. Okada, G. C. Weatherly, and D. W. McComb, *J. Appl. Phys.* **81**, 2185, 1997.
- [70] F. Peiro, A. Cornet, J. R. Morante, A. Georgakilas, C. Wood, and A. Christou, *Appl. Phys. Lett.* **66** 2391, 1995.
- [71] J. Mirecki Millunchick, R. D. Twesten, D. M. Follstaedt, S. R. Lee, E. D. Jones, Y. Zhang, S. P. Ahrenkiel, and A. Mascarenhas, *Appl. Phys. Lett.* **70** 1402, 1997.
- [72] D. D. Perovic, B. Bahierathan, H. Lafontaine, D. C.

- Houghton, and D. W. McComb, *Physica A* **239** 11, 1997.
- [73] N. Liu, J. Tersoff, O. Baklenov, A. L. Holmes Jr., and C. K. Shih, *Phys. Rev. Lett.* **84** 334, 2000.
- [74] J. Tersoff, *Phys. Rev. Lett.* **81** 3183, 1998.
- [75] F. Ratto, F. Rosei, A. Locatelli, S. Cherifi, S. Fontana, S. Heun, P. D. Szkutnik, A. Sgarlate, M. De Crescenzi, and N. Motta, *Appl. Phys. Lett.* **84** 4526, 2004.
- [76] B. A. Joyce, J. L. Sudijono, J. G. Belk, H. Yamaguchi, X. M. Zhang, H. T. Dobbs, A. Zangwill, D. D. Vvedensky, and T. S. Jones, *Jpn. J. Appl. Phys.* **36**, 4111, 1997.
- [77] M. Krishnamurthy, A. Lorke, M. Wassermeier, D. R. M. Williams, and P. M. Petroff, *J. Vac. Sci. Technol. B* **11**, 1384, 1993.
- [78] Mikko Haataja, Jennifer Mahon, Nikolas Provatas and Francois Léonard, *App. Phys. Lett.* **87**, 251901 (2005).
-